


Hybrid one-dimensional photonic crystals containing anisotropic metamaterials: Angle-driven photonic band gaps and angle-driven Tamm plasmon polaritons

Feng Wu ,* Yuchun She, Tingting Zhou, Zhaoming Cheng, and Jianhao Huang

School of Optoelectronic Engineering, *Guangdong Polytechnic Normal University*, Guangzhou 510665, China



(Received 8 May 2024; accepted 22 July 2024; published 2 August 2024)

Herein, we realize a special class of photonic band gaps (PBGs) called angle-driven PBGs in hybrid one-dimensional (1D) photonic crystals (PhCs) composed of alternating anisotropic metamaterial and dielectric layers. At normal incidence, the effective refractive index of the anisotropic metamaterial is designed to be the same as that of the dielectric. Owing to the lack of refractive index contrast, the angle-driven PBG is closed at normal incidence. Under transverse magnetic (TM) polarization, the effective refractive index of the anisotropic metamaterial is angle-dependent since the isofrequency curve (IFC) is an ellipse or a hyperbola. Therefore, the angle-driven PBG under TM polarization is opened at oblique incidence. However, under transverse electric (TE) polarization, the effective refractive index of the anisotropic metamaterial is angle-independent since the IFC is a circle. Therefore, the angle-driven PBG under TE polarization remains closed. In hybrid 1D PhCs composed of alternating elliptical metamaterial and dielectric layers, we realize blueshift angle-driven PBGs under TM polarization. As the incident angle increases, the angle-driven PBG shifts towards shorter wavelengths. Empowered by the blueshift angle-driven PBG, broadband polarization selection and privacy protection can be achieved. In hybrid 1D PhCs composed of alternating hyperbolic metamaterial and dielectric layers, we realize zero-shift angle-driven PBGs under TM polarization. As the incident angle increases, the angle-driven PBG stays almost unchanged. Empowered by the zero-shift angle-driven PBG, wide-angle polarization selection can be achieved. In addition, blueshift and zero-shift angle-driven Tamm plasmon polaritons (TPPs) are realized by placing a metal layer in front of the hybrid 1D PhCs. Our work not only offers an elegant platform to realize angle-driven PBGs and angle-driven TPPs, but also facilitates the development of high-performance polarizers.

DOI: [10.1103/PhysRevA.110.023503](https://doi.org/10.1103/PhysRevA.110.023503)

I. INTRODUCTION

As a category of nanostructures, photonic crystals (PhCs) with periodic refractive index distributions offer us a powerful route to manipulating light [1–3]. Empowered by periodic modulations of refractive index, PhCs can create wavelength ranges called photonic bandgaps (PBGs) in which light is not allowed to propagate [1–3]. Over the past three decades, PBGs in PhCs have been extensively explored in both optical physics [4–14] and devices [15–26]. In optical physics, PBGs in PhCs greatly promote the development of Tamm plasmon polaritons (TPPs) [4–6], Bloch surface modes [7,8], spontaneous emission suppression [9–11], Goos-Hänchen shifts [12], and bound states in the continuum [13,14]. In optical devices, PBGs in PhCs have been utilized to design high-performance reflectors [15], lasers [16,17], fibers [18,19], absorbers [20,21], sensors [22,23], and polarizers [24–26]. According to the Bragg scattering mechanism, PBGs are usually opened at any incident angle [15,27–31]. Such phenomena have been widely observed in one-dimensional (1D) [15,27], two-dimensional (2D) [28,29], and three-dimensional (3D) PhCs [30,31].

Over the past two decades, anisotropic metamaterials have attracted rich attention due to their unique ability to control

light [32–36]. As two main classes of anisotropic metamaterials, elliptical metamaterials [37–42] and hyperbolic metamaterials [27,43–47] have been widely explored. For elliptical metamaterials, all components of effective permittivity and permeability tensors are positive. Hence, isofrequency curves (IFCs) of elliptical metamaterials are ellipses [38,41]. For hyperbolic metamaterials, some components of effective permittivity (or permeability) tensors are positive while the other components are negative. Hence, IFCs of hyperbolic metamaterials are hyperbola [43,44]. In 2011, Hamam *et al.* theoretically discovered a special class of PBGs called angle-driven PBGs in hybrid 1D PhCs composed of alternating elliptical metamaterial and dielectric layers [48]. In Ref. [48], the elliptical metamaterial is mimicked by a 2D dielectric nanowire array. Distinct from conventional PBGs that are usually opened at any incident angle, angle-driven PBGs are closed at normal incidence while are opened at oblique incidence [48]. In 2014, Shen *et al.* theoretically and experimentally observed angle-driven PBGs in hybrid 1D PhCs composed of alternating elliptical metamaterial and dielectric layers [49,50]. In Refs. [49] and [50], the elliptical metamaterial is mimicked by an all-dielectric subwavelength multilayer. Interestingly, researchers found that broadband angular selection can be achieved by cascading dozens of hybrid 1D PhCs with different periodicities [49–56]. In Refs. [48–56], the angle-driven PBGs in hybrid 1D PhCs composed of alternating elliptical metamaterial and dielectric layers strongly

*Contact author: fengwu@gpnu.edu.cn

shift towards shorter wavelengths (i.e., blueshift) as the incident angle increases. The underlying reason is that both the propagating phases in elliptical metamaterial and dielectric layers at a fixed wavelength decrease as the incident angle increases. Consequently, the wavelength satisfying the Bragg condition (i.e., the Bragg wavelength) decreases, giving rise to blueshift angle-driven PBGs. Besides elliptical metamaterials, hyperbolic metamaterials belong to anisotropic metamaterials [43,44]. Different from elliptical metamaterial layer, the propagating phase in hyperbolic metamaterial layer at a fixed wavelength increases as the incident angle increases. A question naturally arises: Could zero-shift angle-driven PBGs be realized in hybrid 1D PhCs composed of alternating hyperbolic metamaterial and dielectric layers? It is known that TPPs occur at the interfaces between a metal layer and a 1D PhC [4,57–59]. Another question naturally arises: Could angle-driven TPPs be realized in heterostructures consisting of a metal layer and a hybrid 1D PhC composed of alternating anisotropic metamaterial and dielectric layers?

In this paper, we discuss angle-driven PBGs in two classes of hybrid 1D PhCs composed of alternating anisotropic metamaterial and dielectric layers. One is hybrid 1D PhCs composed of alternating elliptical metamaterial and dielectric layers. The other is hybrid 1D PhCs composed of alternating hyperbolic metamaterial and dielectric layers. At normal incidence, the effective refractive index of the anisotropic metamaterial is designed to be the same as that of the dielectric. Owing to the lack of refractive index contrast, the angle-driven PBG is closed. At oblique incidence, the effective refractive index of the anisotropic metamaterial under transverse magnetic (TM) polarization become different from that of the dielectric layer. Hence, the angle-driven PBG is opened under TM polarization. Interestingly, at oblique incidence, the effective refractive index of the anisotropic metamaterial under transverse electric (TE) polarization is still the same as that of the dielectric. In other words, the angle-driven PBG remains closed under TE polarization.

As the incident angle increases, both the propagating phases in elliptical metamaterial and dielectric layers under TM polarization at a fixed wavelength decrease. According to the Bragg condition, the angle-driven PBGs in hybrid 1D PhCs composed of alternating elliptical metamaterial and dielectric layers strongly shift towards shorter wavelengths. Empowered by the blueshift angle-driven PBGs, we achieve broadband polarization selection and privacy protection. In addition, we realize blueshift angle-driven TPPs in heterostructures consisting of a metal layer and a hybrid 1D PhC composed of alternating elliptical metamaterial and dielectric layers.

As the incident angle increases, the propagating phase in hyperbolic metamaterial layer under TM polarization at a fixed wavelength increases while that in dielectric layer under TM polarization at a fixed wavelength decreases. When the phase variation of hyperbolic metamaterial layer with respect to the incident angle is compensated with that of dielectric layer with respect to the incident angle, the angle-driven PBG in hybrid 1D PhCs composed of alternating elliptical metamaterial and dielectric layers keeps almost unchanged according to the Bragg condition. Empowered by the zero-shift angle-driven PBGs, we achieve wide-angle polarization

selection. In addition, we realize zero-shift angle-driven TPPs in heterostructures consisting of a metal layer and a hybrid 1D PhC composed of alternating hyperbolic metamaterial and dielectric layers.

The rest of this paper is organized as follows. In Sec. II, we discuss blueshift angle-driven PBGs in hybrid 1D PhCs containing elliptical metamaterials and their applications in broadband polarization selection and privacy protection. In addition, we discuss blueshift angle-driven TPPs in heterostructures consisting of a metal layer and a hybrid 1D PhC containing elliptical metamaterials. In Sec. III, we discuss zero-shift angle-driven PBGs in hybrid 1D PhCs containing hyperbolic metamaterials and their applications in wide-angle polarization selection. In addition, we discuss zero-shift angle-driven TPPs in heterostructures consisting of a metal layer and a hybrid 1D PhC containing hyperbolic metamaterials. Finally, the conclusions are given in Sec. IV.

II. HYBRID 1D PHCS CONTAINING ELLIPTICAL METAMATERIALS: BLUESHIFT ANGLE-DRIVEN PBGS AND TPPS

This section is organized as follows. In Sec. II A, we demonstrate the physical mechanism of the blueshift angle-driven PBGs in hybrid 1D PhCs containing elliptical metamaterials. In Secs. II B and II C, we show two applications of the blueshift angle-driven PBGs: broadband polarization selection and privacy protection. In Sec. II D, we realize blueshift angle-driven TPPs in heterostructures consisting of a metal layer and a hybrid 1D PhC containing elliptical metamaterials.

A. Blueshift angle-driven PBGs in hybrid 1D PhCs containing elliptical metamaterials

Figures 1(a) and 1(b) give the schematics of the conventional PBG and target blueshift angle-driven PBG, respectively. As demonstrated, the conventional PBG under both TM and TE polarizations is opened at any incident angle. Distinct from the conventional PBG, the target angle-driven PBG under TM polarization is closed at normal incidence while that under TM polarization is opened at oblique incidence. In contrast, the target angle-driven PBG under TE polarization keeps closed at both normal and oblique incidences.

To realize a blueshift angle-driven PBG, we propose a hybrid 1D PhC composed of alternating elliptical metamaterial layers (A layers) and dielectric layers (B layers), as schematically depicted in Fig. 2(a). The elliptical metamaterial layers are mimicked by all-dielectric subwavelength multilayers (CD)^M. The whole hybrid 1D PhC can be represented as [(CD)^MB]^N. The materials of C and D layers are selected to be air with a relative permittivity $\epsilon_C = n_C^2 = 1$, and hafnium dioxide (HfO₂) with a relative permittivity $\epsilon_D = n_D^2 = 1.88^2$ [60], respectively. The material of B layer is selected to be silicon dioxide (SiO₂) prepared by glancing angle deposition [61]. The refractive index of SiO₂ prepared by glancing angle deposition can be written as $n_B(\beta) = 1.478 - 1.60836 \times 10^{-4}\beta + 1.66219 \times 10^{-5}\beta^2 - 6.87101 \times 10^{-7}\beta^3$, where β denotes the glancing angle in units of degrees [61]. Here, the glancing angle is set to be $\beta = 87^\circ$. The refractive index of SiO₂ can be calculated as $n_B(87^\circ) = 1.1374$. The incident and

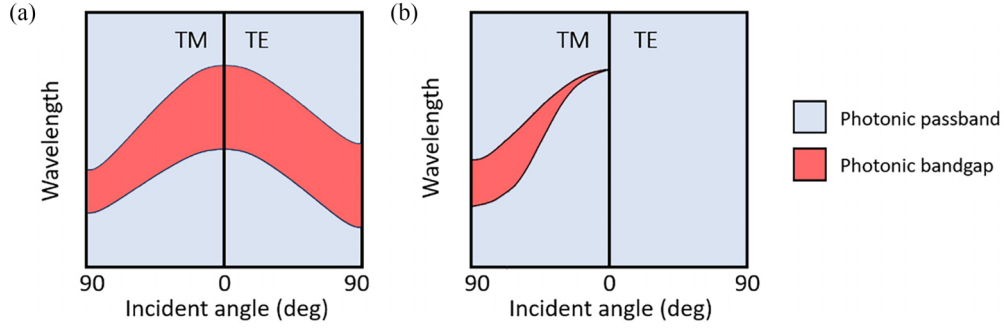


FIG. 1. Schematics of (a) conventional PBG and (b) target blueshift angle-driven PBG.

exit media are air with a relative permittivity $\varepsilon_0 = n_0^2 = 1^2$ and magnesium fluoride (MgF_2) with a relative permittivity $\varepsilon_S = n_S^2 = 1.37^2$ [62], respectively. Suppose that a plane wave launches onto the hybrid 1D PhC $[(\text{CD})^M \text{B}]^N$ in the xOz plane at an incident angle θ_0 .

According to the effective medium approach (EMA), the effective relative permittivity tensor of elliptical metamaterial A can be written as [63]

$$\bar{\varepsilon}_A = \begin{bmatrix} \varepsilon_{Ax} & 0 & 0 \\ 0 & \varepsilon_{Ax} & 0 \\ 0 & 0 & \varepsilon_{Az} \end{bmatrix}, \quad (1)$$

where

$$\varepsilon_{Ax} = p\varepsilon_C + (1-p)\varepsilon_D, \quad (2a)$$

$$1/\varepsilon_{Az} = p/\varepsilon_C + (1-p)/\varepsilon_D. \quad (2b)$$

Here, $p = d_C/(d_C + d_D)$ denotes the filling ratio of dielectric C in the elliptical metamaterial layer. For elliptical metamaterial, we have $\varepsilon_{Ax} > 0$, $\varepsilon_{Az} > 0$, and $\varepsilon_{Ax} \neq \varepsilon_{Az}$.

The equations of the IFCs of elliptical metamaterial A under TM and TE polarizations can be expressed

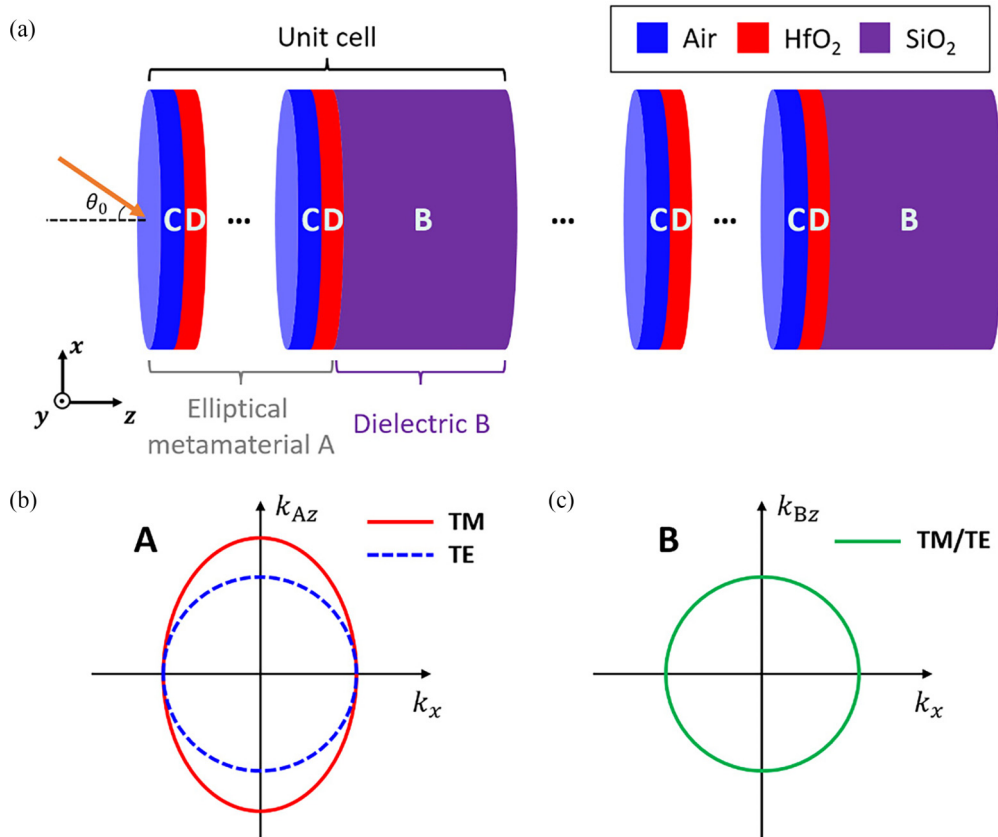


FIG. 2. (a) Schematic of the hybrid 1D PhC composed of alternating elliptical metamaterial layers (A layers) and dielectric layers (B layers). The elliptical metamaterial layers are mimicked by all-dielectric subwavelength multilayers $(\text{CD})^M$. Schematics of the IFCs of (b) elliptical metamaterial A and (c) dielectric B under TM and TE polarizations.

as [44]

$$\frac{k_x^2}{\varepsilon_{Az}} + \frac{k_{Az}^2}{\varepsilon_{Ax}} = k_0^2 \quad (\text{TM polarization}), \quad (3a)$$

$$\frac{k_x^2}{\varepsilon_{Ax}} + \frac{k_{Az}^2}{\varepsilon_{Ax}} = k_0^2 \quad (\text{TE polarization}), \quad (3b)$$

where $k_x = k_0 \sin\theta$ denotes tangential component of the wave vector, k_{Az} denotes the normal component of the wave vector in elliptical metamaterial A, and $k_0 = 2\pi/\lambda_0$ denotes the wave vector in air with λ_0 being the wavelength in air. From Eq. (3a), the IFC of elliptical metamaterial A under TM polarization is an ellipse, as shown by the red solid line in Fig. 2(b). From Eq. (3b), the IFC of elliptical metamaterial A under TE polarization is a circle, as shown by the blue dashed line in Fig. 2(b).

Similarly, the equations of the IFCs of dielectric B under TM and TE polarizations can be expressed as [44]

$$\frac{k_x^2}{\varepsilon_B} + \frac{k_{Bz}^2}{\varepsilon_B} = k_0^2 \quad (\text{TM and TE polarizations}), \quad (4)$$

where k_{Bz} denotes the normal component of the wave vector in dielectric B. From Eq. (4), the IFCs of dielectric B under TM and TE polarizations are both circles, as shown by the green solid line in Fig. 2(c).

Under TM polarization, elliptical metamaterial A can be treated as an anisotropic medium since its IFC is an ellipse. The effective refractive index of elliptical metamaterial A n_A^{TM} depends on the incident angle θ_0 , i.e., [64]

$$n_A^{\text{TM}}(\theta_0) = \frac{1}{\sqrt{\frac{\cos^2[\theta_A^{\text{TM}}(\theta_0)]}{\varepsilon_{Ax}} + \frac{\sin^2[\theta_A^{\text{TM}}(\theta_0)]}{\varepsilon_{Az}}}}. \quad (5)$$

In Eq. (5), $\theta_A^{\text{TM}}(\theta_0)$ denotes the refractive angle in elliptical metamaterial A, which satisfying the Snell's law

$$n_A^{\text{TM}}(\theta_0) \sin[\theta_A^{\text{TM}}(\theta_0)] = n_0 \sin\theta_0. \quad (6)$$

In Eq. (6), $n_0 = 1$ denotes the refractive index of the incident medium.

At normal incidence ($\theta_0 = 0^\circ$), we have $\theta_A^{\text{TM}}(0^\circ) = 0^\circ$. Substituting $\theta_A^{\text{TM}}(0^\circ) = 0^\circ$ into Eq. (5), we obtain $n_A^{\text{TM}}(0^\circ) = \sqrt{\varepsilon_{Ax}}$. To close the angle-driven PBG at normal incidence, we set

$$n_A^{\text{TM}}(0^\circ) = \sqrt{\varepsilon_{Ax}} = n_B = 1.1374. \quad (7)$$

Combining Eqs. (2a) and (7), the filling ratio of dielectric C can be calculated as

$$p = \frac{\varepsilon_B - \varepsilon_D}{\varepsilon_C - \varepsilon_D} = 0.8841. \quad (8)$$

Then, combining Eqs. (5) and (6), the dependence of the effective refractive index of elliptical metamaterial A under TM polarization on the incident angle $n_A^{\text{TM}}(\theta_0)$ can be solved, as shown by the red solid line in Fig. 3. At normal incidence, $n_A^{\text{TM}}(0^\circ) = n_B = 1.1374$. Therefore, no PBG is opened due to the lack of the refractive index contrast. At oblique incidence, $n_A^{\text{TM}}(\theta_0) \neq n_B = 1.1374$. Therefore, a PBG is opened under TM polarization empowered by the refractive index contrast. As the incident angle increases from 0° to $\sim 90^\circ$, the refractive index contrast gradually increases since n_A^{TM} decreases from 1.1374 to 1.0524. As a result, the PBG under TM polarization

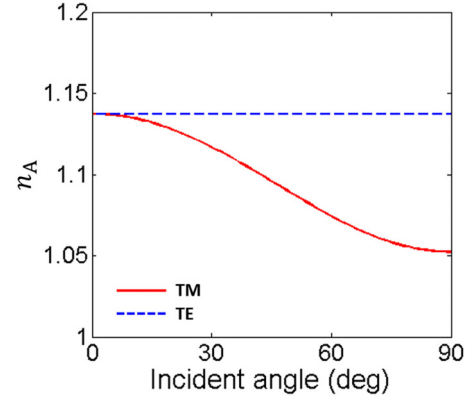


FIG. 3. Dependences of the effective refractive indices of elliptical metamaterial A on the incident angle under TM and TE polarizations.

is gradually enlarged. This PBG driven by the incident angle can be called as the angle-driven PBG.

Under TE polarization, elliptical metamaterial A can be treated as an isotropic medium since its IFC is a circle. The effective refractive index of elliptical metamaterial A n_A^{TE} is independent of the incident angle θ_0 , i.e., [64]

$$n_A^{\text{TE}} = \sqrt{\varepsilon_{Ax}} = 1.1374. \quad (9)$$

As shown by the blue dashed line in Fig. 3, $n_A^{\text{TE}} = n_B = 1.1374$ is always satisfied at any incident angle. Therefore, no PBG is opened under TE polarization at both normal and oblique incidences.

According to the Bragg scattering theory, the Bragg condition of the first-order angle-driven PBG under TM polarization takes the following form [65]:

$$\begin{aligned} \Phi(\lambda_{\text{Brg}}^{\text{TM}}, \theta_0) &= \Phi_A(\lambda_{\text{Brg}}^{\text{TM}}, \theta_0) + \Phi_B(\lambda_{\text{Brg}}^{\text{TM}}, \theta_0) \\ &= k_{Az}(\lambda_{\text{Brg}}^{\text{TM}}, \theta_0)d_A + k_{Bz}(\lambda_{\text{Brg}}^{\text{TM}}, \theta_0)d_B = \pi, \end{aligned} \quad (10)$$

where Φ denotes the propagating phase in a unit cell of the hybrid 1D PhC, $\lambda_{\text{Brg}}^{\text{TM}}$ denotes the Bragg wavelength of the first-order PBG under TM polarization, d_A denotes the thickness of the elliptical metamaterial layer, and d_B denotes the thickness of the dielectric layer.

Substituting Eqs. (3a) and (4) into Eq. (10), we can obtain the solution of Eq. (10), i.e.,

$$\lambda_{\text{Brg}}^{\text{TM}}(\theta_0) = 2 \left(\sqrt{\varepsilon_{Ax} - \frac{\varepsilon_{Ax}}{\varepsilon_{Az}} \sin^2\theta_0} d_A + \sqrt{\varepsilon_B - \sin^2\theta_0} d_B \right). \quad (11)$$

Since $\varepsilon_{Ax} > 0$ and $\varepsilon_{Az} > 0$, the Bragg wavelength of the first-order PBG under TM polarization $\lambda_{\text{Brg}}^{\text{TM}}$ decreases as the incident angle θ_0 increases. Therefore, the angle-driven PBG under TM polarization shifts towards shorter wavelengths (i.e., blueshift). In our design, the Bragg wavelength of the first-order angle-driven PBG at normal incidence is set to be $\lambda_{\text{Brg}}^{\text{TM}}(0^\circ) = 2400$ nm. Also, the thickness of the elliptical metamaterial layer is set to be $d_A = 440$ nm. To ensure the accuracy of the EMA, the number of periods in elliptical metamaterial layer is chosen to be $M = 40$. Since $p = 0.8841$, the thicknesses of C and D layers in the elliptical metamaterial layer can be calculated as $d_C = pd_A/40 =$

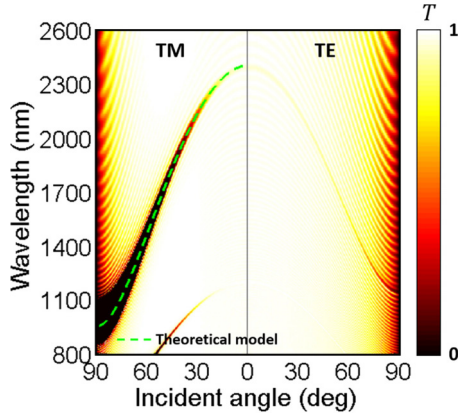


FIG. 4. Dependence of the transmittance spectrum of the hybrid 1D PhC $[(\text{CD})^{40} \text{B}]^{40}$ on the incident angle under TM and TE polarizations. Green dashed line represents the dependence of the Bragg wavelength predicted by the theoretical model on the incident angle.

9.73 nm and $d_D = (1-p)d_A/40 = 1.27$ nm, respectively. The thickness of a unit cell in the elliptical metamaterial layer is only $d_{A,\text{Unit}} = d_C + d_D = 11.00$ nm $\approx 0.0046\lambda_{\text{Brg}}^{\text{TM}}(0^\circ)$, indicates that the deep subwavelength condition is satisfied. Substituting $\lambda_{\text{Brg}}^{\text{TM}}(0^\circ) = 2400$ nm and $d_A = 440$ nm into Eq. (11), the thickness of the dielectric layer can be obtained, i.e., $d_B = 615.04$ nm.

To realize a deep angle-driven PBG, the number of periods in the hybrid 1D PhC is chosen to be $N = 40$. According to the transfer matrix method [64], we numerically calculate the dependence of the transmittance spectrum of the hybrid 1D PhC $[(\text{CD})^{40} \text{B}]^{40}$ on the incident angle under TM and TE polarizations, as depicted in Fig. 4. As demonstrated, a blueshift angle-driven PBG occurs. Under TM polarization, the angle-driven PBG is closed at normal incidence while it is opened at oblique incidence. Under TE polarization, the angle-driven PBG keeps closed at both normal and oblique incidences. Also, we calculate the dependence of the Bragg wavelength predicted by the theoretical model [Eq. (11)] on the incident angle, as shown in the green dashed line. As

demonstrated, the theoretical model agrees well with the numerical results.

Figure 5(a) gives the transmittance spectra of the hybrid 1D PhC $[(\text{CD})^{40} \text{B}]^{40}$ under TM polarization at normal ($\theta_0 = 0^\circ$) and oblique ($\theta_0 = 45^\circ$) incidences. Clearly, the angle-driven PBG is closed at normal incidence while it is opened at oblique incidence. At $\theta_0 = 45^\circ$, the angle-driven PBG ranges from 1777.62 to 1890.87 nm. Figure 5(b) gives the transmittance spectra of the hybrid 1D PhC $[(\text{CD})^{40} \text{B}]^{40}$ under TE polarization at normal ($\theta_0 = 0^\circ$) and oblique ($\theta_0 = 45^\circ$) incidences. Clearly, the angle-driven PBG is closed at both normal and oblique incidences. Therefore, the angle-driven PBG exhibits a superior polarization-dependent property. Empowered by the superior polarization-dependent property of the blueshift angle-driven PBG, broadband polarization selection can be achieved.

B. Broadband polarization selection empowered by blueshift angle-driven PBGs

In this subsection, we utilize the superior polarization-dependent property of the blueshift angle-driven PBG to achieve broadband polarization selection. The materials and thicknesses of the hybrid 1D PhC are the same as those in Sec. II A. The incident and exit media are air with a relative permittivity $\epsilon_0 = n_0^2 = 1^2$ and MgF_2 with a relative permittivity $\epsilon_S = n_S^2 = 1.37^2$ [62], respectively. To obtain high polarization selection ratio, we consider two cases: $\theta_0 = 60^\circ$ and $\theta_0 = 80^\circ$.

Figure 6(a) gives the transmittance spectra of the hybrid 1D PhC $[(\text{CD})^{40} \text{B}]^{40}$ under TM and TE polarizations at $\theta_0 = 60^\circ$. Under TM polarization, the angle-driven PBG is opened. Specifically, the angle-driven PBG ranges from 1396.00 to 1545.10 nm. The width of the angle-driven PBG reaches 149.10 nm. The transmittance inside the angle-driven PBG is near zero. Under TE polarization, the angle-driven PBG is closed. Therefore, the transmittance keeps higher than 0.75. Figure 6(b) gives the polarization selection ratio spectrum of the hybrid 1D PhC $[(\text{CD})^{40} \text{B}]^{40}$ at $\theta_0 = 60^\circ$. The polarization selection ratio inside the angle-driven PBG is quite high. At the wavelength of 1465.22 nm, the polarization selection ratio

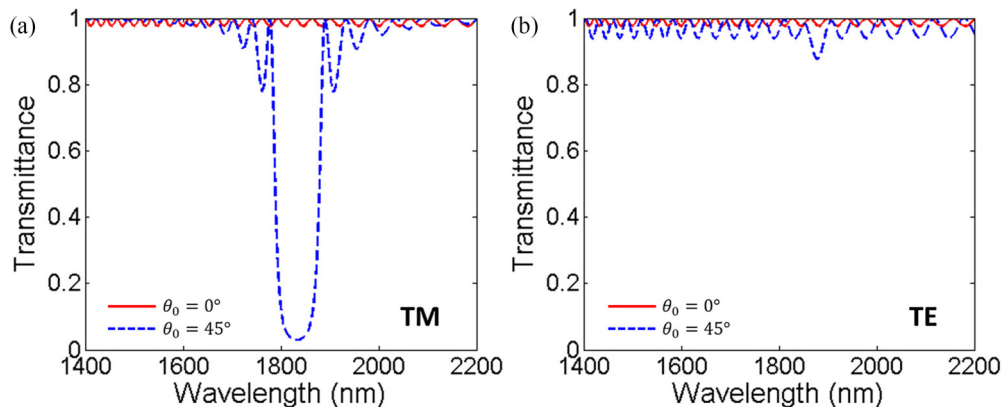


FIG. 5. (a) Transmittance spectra of the hybrid 1D PhC $[(\text{CD})^{40} \text{B}]^{40}$ under TM polarization at normal ($\theta_0 = 0^\circ$) and oblique ($\theta_0 = 45^\circ$) incidences. (b) Transmittance spectra of the hybrid 1D PhC $[(\text{CD})^{40} \text{B}]^{40}$ under TE polarization at normal ($\theta_0 = 0^\circ$) and oblique ($\theta_0 = 45^\circ$) incidences.

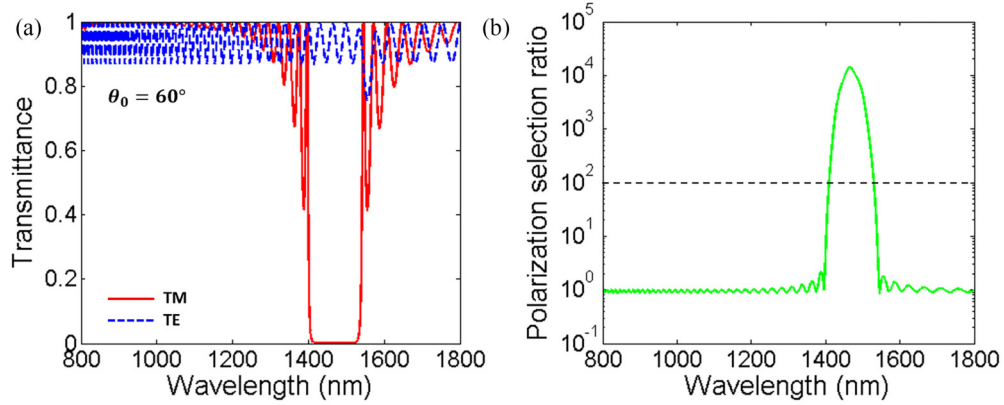


FIG. 6. (a) Transmittance spectra of the hybrid 1D PhC [(CD)⁴⁰B]⁴⁰ under TM and TE polarizations at $\theta_0 = 60^\circ$. (b) Polarization selection ratio spectrum of the hybrid 1D PhC [(CD)⁴⁰B]⁴⁰ at $\theta_0 = 60^\circ$. The black dashed line represents the polarization selection ratio equal to 10^2 .

achieves its maximum 1.41×10^4 . We define the wavelength range where the polarization selection ratio is higher than 10^2 as the operating wavelength range. The operating wavelength range is from 1409.62 to 1529.17 nm. The width of the operating wavelength range reaches 119.55 nm.

Figure 7(a) gives the transmittance spectra of the hybrid 1D PhC [(CD)⁴⁰B]⁴⁰ under TM and TE polarizations at $\theta_0 = 80^\circ$. Under TM polarization, the angle-driven PBG is opened. Specifically, the angle-driven PBG ranges from 932.43 to 1168.90 nm. The width of the angle-driven PBG reaches 236.47 nm, which is wider than that in the case of $\theta_0 = 60^\circ$. The transmittance inside the angle-driven PBG is near zero. Under TE polarization, the angle-driven PBG is closed. Therefore, the transmittance keeps higher than 0.34. Fig. 7(b) gives the polarization selection ratio spectrum of the hybrid 1D PhC [(CD)⁴⁰B]⁴⁰ at $\theta_0 = 80^\circ$. The polarization selection ratio inside the angle-driven PBG is quite high. At the wavelength of 1033.12 nm, the polarization selection ratio achieves its maximum 1.16×10^{11} , which is much higher than that in the case of $\theta_0 = 60^\circ$. The operating wavelength range is from 934.72 to 1165.65 nm. The width of the operating wavelength range reaches 230.93 nm. As the incident

angle increases from 60° to 80° , the width of the operating wavelength range becomes larger since the width of the angle-driven PBG becomes larger. Nevertheless, the transmittance under TE polarization becomes lower due to the stronger impedance mismatch between the incident medium and hybrid 1D PhC.

C. Broadband privacy protection empowered by blueshift angle-driven PBGs

Recently, a kind of narrow-view display technology called privacy protection have attracted rich attention [66,67]. In this subsection, we utilize the blueshift angle-driven PBG to achieve broadband privacy protection under TM polarization. Here, we redesign the hybrid 1D PhC to achieve high-performance privacy protection. The materials of C and D layers are selected to be air with a relative permittivity $\epsilon_C = n_C^2 = 1$, and HfO₂ with a relative permittivity $\epsilon_D = n_D^2 = 1.88^2$ [60], respectively. The material of B layer is selected to be MgF₂ with a relative permittivity $\epsilon_B = n_B^2 = 1.37^2$ [62]. The incident and exit media are air with a relative permittivity

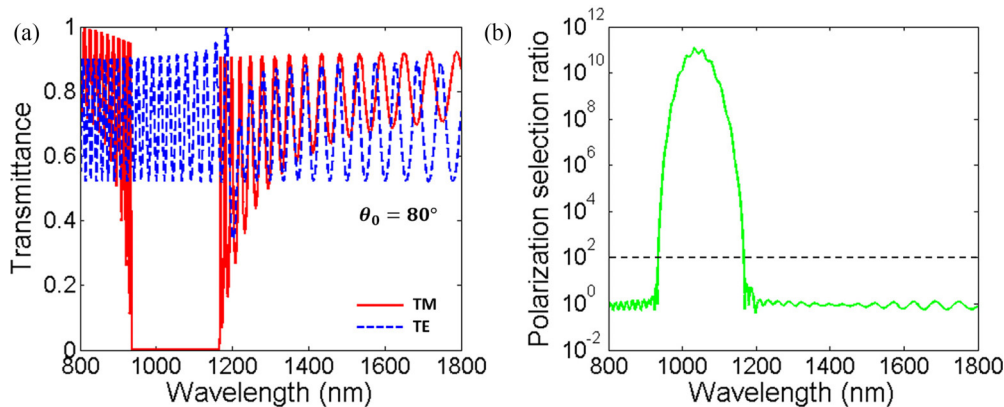


FIG. 7. (a) Transmittance spectra of the hybrid 1D PhC [(CD)⁴⁰B]⁴⁰ under TM and TE polarizations at $\theta_0 = 80^\circ$. (b) Polarization selection ratio spectrum of the hybrid 1D PhC [(CD)⁴⁰B]⁴⁰ at $\theta_0 = 80^\circ$. The black dashed line represents the polarization selection ratio equal to 10^2 .

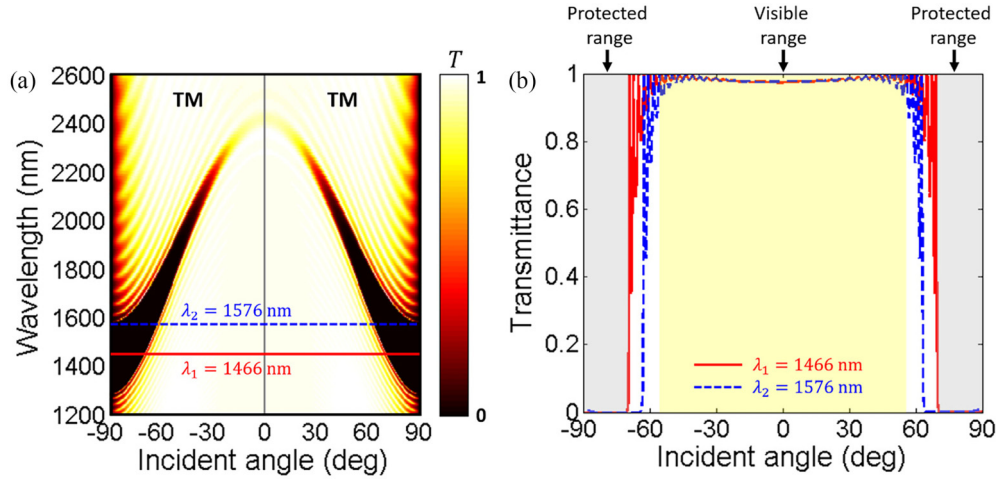


FIG. 8. (a) Dependence of the transmittance spectrum of the hybrid 1D PhC $[(\text{CD})^{40}\text{B}]^{30}$ on the incident angle under TM polarization. (b) Transmittance angular spectra of the hybrid 1D PhC $[(\text{CD})^{40}\text{B}]^{30}$ under TM polarization at $\lambda_1 = 1466$ nm and $\lambda_2 = 1576$ nm.

$\varepsilon_0 = n_0^2 = 1^2$ and MgF_2 with a relative permittivity $\varepsilon_S = n_S^2 = 1.37^2$, respectively. According to Eq. (8), the filling ratio of dielectric C can be obtained as $p = (\varepsilon_B - \varepsilon_D)/(\varepsilon_C - \varepsilon_D) = 0.6540$. The Bragg wavelength of the first-order angle-driven PBG at normal incidence is set to be $\lambda_{\text{Brag}}^{\text{TM}}(0^\circ) = 2400$ nm. Also, the thickness of the elliptical metamaterial layer is set to be $d_A = 440$ nm. To ensure the accuracy of the EMA, the number of periods in elliptical metamaterial layer is chosen to be $M = 40$. Since $p = 0.6540$, the thicknesses of C and D layers in the elliptical metamaterial layer can be calculated as $d_C = pd_A/40 = 7.19$ nm and $d_D = (1-p)d_A/40 = 3.81$ nm, respectively. The thickness of a unit cell in the elliptical metamaterial layer is only $d_{A,\text{Unit}} = d_C + d_D = 11.00$ nm $\approx 0.0046\lambda_{\text{Brag}}^{\text{TM}}(0^\circ)$, indicates that the deep subwavelength condition is satisfied. Substituting $\lambda_{\text{Brag}}^{\text{TM}}(0^\circ) = 2400$ nm and $d_A = 440$ nm into Eq. (11), the thickness of the dielectric layer can be obtained, i.e., $d_B = 435.91$ nm.

To realize a deep angle-driven PBG, the number of periods in the hybrid 1D PhC is chosen to be $N = 30$. According to the transfer matrix method [64], we numerically calculate the dependence of the transmittance spectrum of the hybrid 1D PhC $[(\text{CD})^{40}\text{B}]^{30}$ on the incident angle under TM polarization, as depicted in Fig. 8(a). Notice that both the left and right panels denote TM polarization. The left panel denotes negative incident angles while the right one denotes positive incident angles. As demonstrated, a blueshift angle-driven PBG occurs. Therefore, privacy protection can be achieved in the wavelength range between $\lambda_1 = 1466$ nm and $\lambda_2 = 1576$ nm. Figure 8(b) gives the transmittance angular spectra of the hybrid 1D PhC $[(\text{CD})^{40}\text{B}]^{30}$ under TM polarization at $\lambda_1 = 1466$ nm and $\lambda_2 = 1576$ nm. In the wavelength range from 1466 to 1576 nm, the transmittance keeps higher than 0.9 in the angle range $(-55^\circ, 55^\circ)$. This angle range can be called the visible range, as shown by the yellow region. In the wavelength range from 1466 to 1576 nm, the transmittance keeps lower than 0.01 in the angle ranges $(-90^\circ, -70^\circ)$ and $(70^\circ, 90^\circ)$. These angle ranges can be called as the protected ranges, as shown by the grey regions.

D. Blueshift angle-driven TPPs in heterostructures consisting of a metal layer and a hybrid 1D PhC containing elliptical metamaterials

In this subsection, we realize a blueshift angle-driven TPP in a heterostructure consisting of a metal layer and a hybrid 1D PhC containing elliptical metamaterials with a blueshift angle-driven PBG. Figures 9(a) and 9(b) give the schematics of the conventional TPP and target blueshift angle-driven TPP, respectively. Since the conventional PBG under both TM and TE polarizations is usually opened at any incident angle, the corresponding TPP under both TM and TE polarizations usually occurs at any incident angle. This class of TPPs can be called as conventional TPPs. Since the blueshift angle-driven PBG under TM polarization is closed at normal incidence while that under TM polarization is opened at oblique incidence, the corresponding TPP under TM polarization does not occur at normal incidence while that under TM polarization occurs at oblique incidence. Also, the corresponding TPP under TE polarization does not occur at both normal and oblique incidences since the PBG under TE polarization is closed at both normal and oblique incidences. As incident angle increases, the TPP under TM polarization shifts towards shorter wavelengths since the PBG under TM polarization shifts towards shorter wavelengths. This class of TPPs can be called the blueshift angle-driven TPPs.

To realize a blueshift angle-driven TPP, we propose a heterostructure consisting of a metal layer (M layer) and a hybrid 1D PhC composed of alternating elliptical metamaterial layers (A layers) and dielectric layers (B layers), as schematically depicted in Fig. 10(a). The whole heterostructure can be represented as $M[(\text{CD})^M\text{B}]^N$. The material of M layer is selected to be indium tin oxide (ITO) [68]. The relative permittivity of ITO can be described by the Drude model, i.e., $\varepsilon_M = \varepsilon_{M,\text{inf}} - \omega_{M,p}^2/(\omega^2 + i\gamma_M\omega)$, where $\varepsilon_{M,\text{inf}} = 3.9$ denotes the high-frequency relative permittivity, $\hbar\omega_{M,p} = 2.48$ eV denotes the plasma energy, and $\hbar\gamma_M = 0.016$ eV denotes the damping energy [68]. The materials of C and D layers are selected to be air with a relative permittivity $\varepsilon_C = n_C^2 = 1$, and

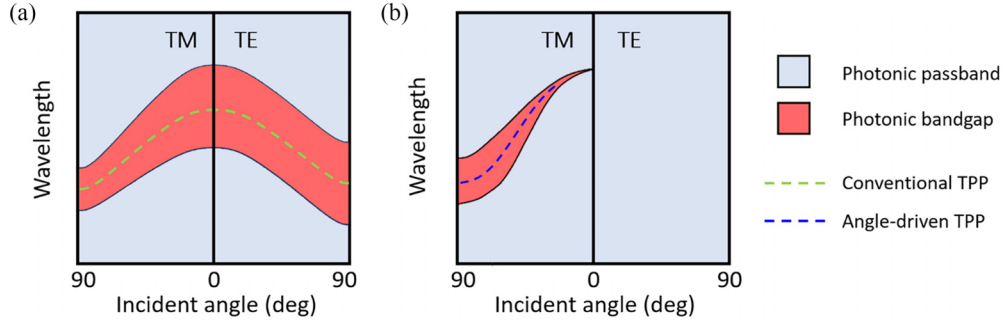


FIG. 9. Schematics of (a) conventional TPP and (b) target blueshift angle-driven TPP.

HfO₂ with a relative permittivity $\varepsilon_D = n_D^2 = 1.88^2$ [60], respectively. The material of B layer is selected to be MgF₂ with a relative permittivity $\varepsilon_B = n_B^2 = 1.37^2$ [62]. The incident and exit media are air with a relative permittivity $\varepsilon_0 = n_0^2 = 1^2$ and MgF₂ with a relative permittivity $\varepsilon_S = n_S^2 = 1.37^2$, respectively.

Now, we design the heterostructure to realize a blueshift angle-driven TPP. The thickness of M layer is set to be $d_M = 110$ nm. According to Eq. (8), the filling ratio of dielectric C can be obtained as $p = (\varepsilon_B - \varepsilon_D)/(\varepsilon_C - \varepsilon_D) = 0.6540$. The Bragg wavelength of the first-order angle-driven PBG at normal incidence is set to be $\lambda_{\text{Brg}}^{\text{TM}}(0^\circ) = 2400$ nm. Also, the thickness of the elliptical metamaterial layer is set to be $d_A = 300$ nm. To ensure the accuracy of the EMA, the number of periods in elliptical metamaterial layer is chosen

to be $M = 40$. Since $p = 0.6540$, the thicknesses of C and D layers in the elliptical metamaterial layer can be calculated as $d_C = pd_A/40 = 4.905$ nm and $d_D = (1-p)d_A/40 = 2.595$ nm, respectively. The thickness of a unit cell in the elliptical metamaterial layer is only $d_{\text{A,Unit}} = d_C + d_D = 7.50$ nm $\approx 0.0031\lambda_{\text{Brg}}^{\text{TM}}(0^\circ)$, indicates that the deep subwavelength condition is satisfied. Substituting $\lambda_{\text{Brg}}^{\text{TM}}(0^\circ) = 2400$ nm and $d_A = 300$ nm into Eq. (11), the thickness of the dielectric layer can be obtained, i.e., $d_B = 575.91$ nm. To realize a blueshift angle-driven TPP, a wide blueshift angle-driven PBG is required. Hence, the number of periods in the hybrid 1D PhC is chosen to be $N = 15$. According to the transfer matrix method [64], we numerically calculate the dependence of the transmittance spectrum of the heterostructure $M[(\text{CD})^{40}\text{B}]^{15}$ on the incident angle under TM and TE polarizations, as depicted in Fig. 10(b). The green dashed lines represent the dependences of the wavelengths of two band edges on the incident angle. As demonstrated, a blueshift angle-driven TPP occurs. Under TM polarization, the angle-driven TPP does not occur at normal incidence. As the incident angle increases to 16° , the angle-driven TPP occurs at 2364.76 nm. As the incident angle continues to increase to $\sim 90^\circ$, the angle-driven TPP strongly shifts to 1571.38 nm. Under TE polarization, the angle-driven TPP does not occur at both normal and oblique incidences.

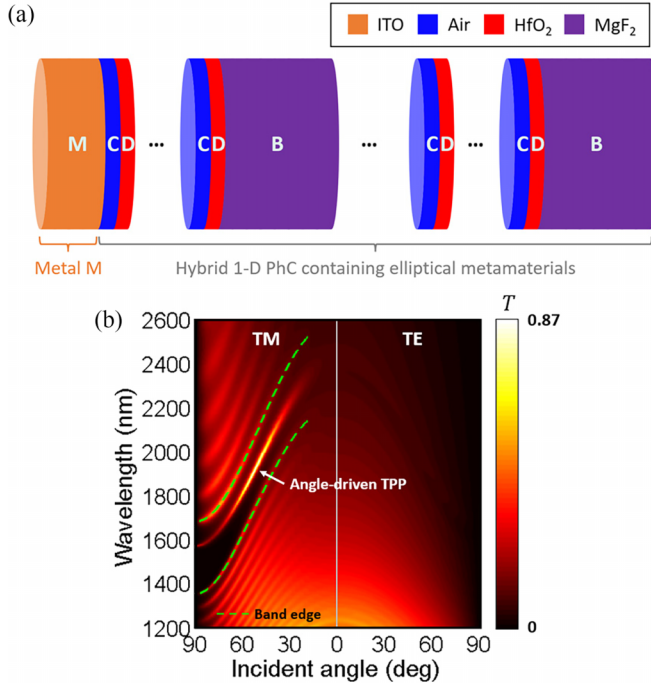


FIG. 10. (a) Schematic of the heterostructure consisting of a metal layer (M layer) and a hybrid 1D PhC composed of alternating elliptical metamaterial layers (A layers) and dielectric layers (B layers). (b) Dependence of the transmittance spectrum of the heterostructure $M[(\text{CD})^{40}\text{B}]^{15}$ on the incident angle under TM and TE polarizations. Green dashed lines represent the dependences of the wavelengths of two band edges on the incident angle.

Figure 11(a) gives the transmittance spectra of the heterostructure $M[(\text{CD})^{40}\text{B}]^{15}$ under TM polarization at normal ($\theta_0 = 0^\circ$) and oblique ($\theta_0 = 50^\circ$) incidences. Clearly, the angle-driven TPP does not occur at normal incidence while occurs at oblique incidence. At $\theta_0 = 50^\circ$, the angle-driven TPP occurs at 1954.40 nm. Figure 11(b) gives the transmittance spectra of the heterostructure $M[(\text{CD})^{40}\text{B}]^{15}$ under TE polarization at normal ($\theta_0 = 0^\circ$) and oblique ($\theta_0 = 50^\circ$) incidences. Clearly, the angle-driven TPP does not occur at both normal and oblique incidences. Therefore, the angle-driven TPP exhibits a superior polarization-dependent property. Empowered by the superior polarization-dependent property of the blueshift angle-driven TPP, narrowband polarization selection can be achieved.

III. HYBRID 1D PHCs CONTAINING HYPERBOLIC METAMATERIALS: ZERO-SHIFT ANGLE-DRIVEN PBGS AND TPPs

This section is organized as follows. In Sec. III A, we demonstrate the physical mechanism of the zero-shift

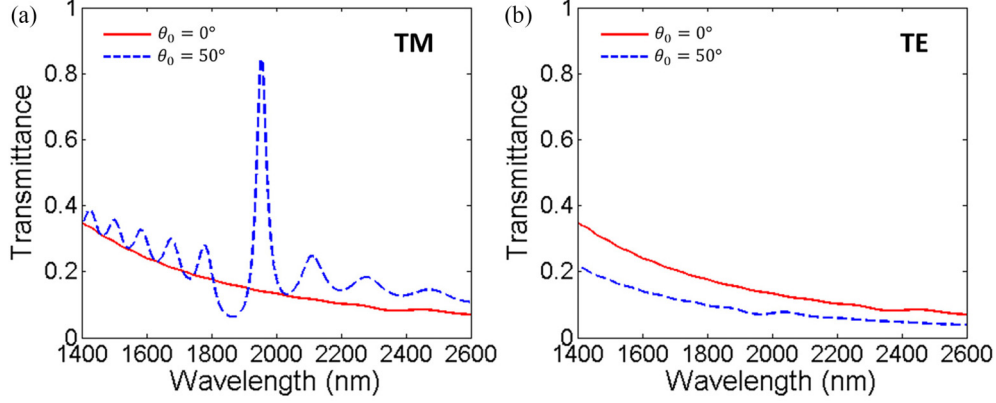


FIG. 11. (a) Transmittance spectra of the heterostructure $M[(CD)^{40}B]^{15}$ under TM polarization at normal ($\theta_0 = 0^\circ$) and oblique ($\theta_0 = 50^\circ$) incidences. (b) Transmittance spectra of the heterostructure $M[(CD)^{40}B]^{15}$ under TE polarization at normal ($\theta_0 = 0^\circ$) and oblique ($\theta_0 = 50^\circ$) incidences.

angle-driven PBGs in hybrid 1D PhCs containing hyperbolic metamaterials. In Sec. III B, we show an application of the zero-shift angle-driven PBGs: wide-angle polarization selection. In Sec. III C, we realize zero-shift angle-driven TPPs in heterostructures consisting of a metal layer and a hybrid 1D PhC containing hyperbolic metamaterials.

A. Zero-shift angle-driven PBGs in hybrid 1D PhCs containing hyperbolic metamaterials

To realize a zero-shift angle-driven PBG, we propose a hybrid 1D PhC composed of alternating hyperbolic metamaterial layers (A layers) and dielectric layers (B layers), as schematically depicted in Fig. 12(a). The hyperbolic metamaterial layers are mimicked by dielectric-metal subwavelength multilayers $(CD)^M$. The whole hybrid 1D PhC can be represented as $[(CD)^M B]^N$. The material of the C layer is selected to be silicon (Si) with a relative permittivity $\epsilon_C = n_C^2 = 3.48^2$ [62]. Initially, we ignore the dispersion and loss of the metal. The material of D layer is selected to be a nondispersive lossless metal with a relative permittivity $\epsilon_D = -5$. In the Appendix, we investigate the effects of the dispersion and loss of the metal on the zero-shift angle-driven PBG and zero-shift angle-driven TPP. The material of the B layer is selected to be MgF_2 with a relative permittivity $\epsilon_B = n_B^2 = 1.37^2$ [62]. The incident and exit media are air with a relative permittivity $\epsilon_0 = n_0^2 = 1^2$ and MgF_2 with a relative permittivity $\epsilon_S = n_S^2 = 1.37^2$ [62], respectively. Suppose that a plane wave launches onto the hybrid 1D PhC $[(CD)^M B]^N$ in the xOz plane at an incident angle θ_0 .

According to the EMA, the effective relative permittivity tensor of hyperbolic metamaterial A can be written as [63]

$$\epsilon_A = \begin{bmatrix} \epsilon_{Ax} & 0 & 0 \\ 0 & \epsilon_{Ax} & 0 \\ 0 & 0 & \epsilon_{Az} \end{bmatrix}, \quad (12)$$

where

$$\epsilon_{Ax} = p\epsilon_C + (1-p)\epsilon_D, \quad (13a)$$

$$1/\epsilon_{Az} = p/\epsilon_C + (1-p)/\epsilon_D. \quad (13b)$$

Here, $p = d_C/(d_C + d_D)$ denotes the filling ratio of dielectric C in the hyperbolic metamaterial layer. For type-I hyperbolic metamaterial, we have $\epsilon_{Ax} > 0$ and $\epsilon_{Az} < 0$.

The equations of the IFCs of hyperbolic metamaterial A under TM and TE polarizations can be expressed as [44]

$$\frac{k_x^2}{\epsilon_{Az}} + \frac{k_{Az}^2}{\epsilon_{Ax}} = k_0^2 \quad (\text{TM polarization}), \quad (14a)$$

$$\frac{k_x^2}{\epsilon_{Ax}} + \frac{k_{Az}^2}{\epsilon_{Ax}} = k_0^2 \quad (\text{TE polarization}), \quad (14b)$$

where $k_x = k_0 \sin\theta$ denotes tangential component of the wave vector, k_{Az} denotes the normal component of the wave vector in hyperbolic metamaterial A, and $k_0 = 2\pi/\lambda_0$ denotes the wave vector in air with λ_0 being the wavelength in air. From Eq. (14a), the IFC of hyperbolic metamaterial A under TM polarization is a hyperbola, as shown by the red solid lines in Fig. 12(b). From Eq. (14b), the IFC of hyperbolic metamaterial A under TE polarization is a circle, as shown by the blue dashed line in Fig. 12(b).

Similarly, the equations of the IFCs of dielectric B under TM and TE polarizations can be expressed as [44]

$$\frac{k_x^2}{\epsilon_B} + \frac{k_{Bz}^2}{\epsilon_B} = k_0^2 \quad (\text{TM and TE polarizations}), \quad (15)$$

where k_{Bz} denotes the normal component of the wave vector in dielectric B. From Eq. (15), the IFCs of dielectric B under TM and TE polarizations are both circles, as shown by the green solid line in Fig. 12(c).

Under TM polarization, hyperbolic metamaterial A can be treated as an anisotropic medium since its IFC is a hyperbola. The effective refractive index of hyperbolic metamaterial A n_A^{TM} depends on the incident angle θ_0 , i.e., [64]

$$n_A^{\text{TM}}(\theta_0) = \frac{1}{\sqrt{\frac{\cos^2[\theta_A^{\text{TM}}(\theta_0)]}{\epsilon_{Ax}} + \frac{\sin^2[\theta_A^{\text{TM}}(\theta_0)]}{\epsilon_{Az}}}}. \quad (16)$$

In Eq. (16), $\theta_A^{\text{TM}}(\theta_0)$ denotes the refractive angle in hyperbolic metamaterial A, which satisfying the Snell's law

$$n_A^{\text{TM}}(\theta_0) \sin[\theta_A^{\text{TM}}(\theta_0)] = n_0 \sin\theta_0. \quad (17)$$

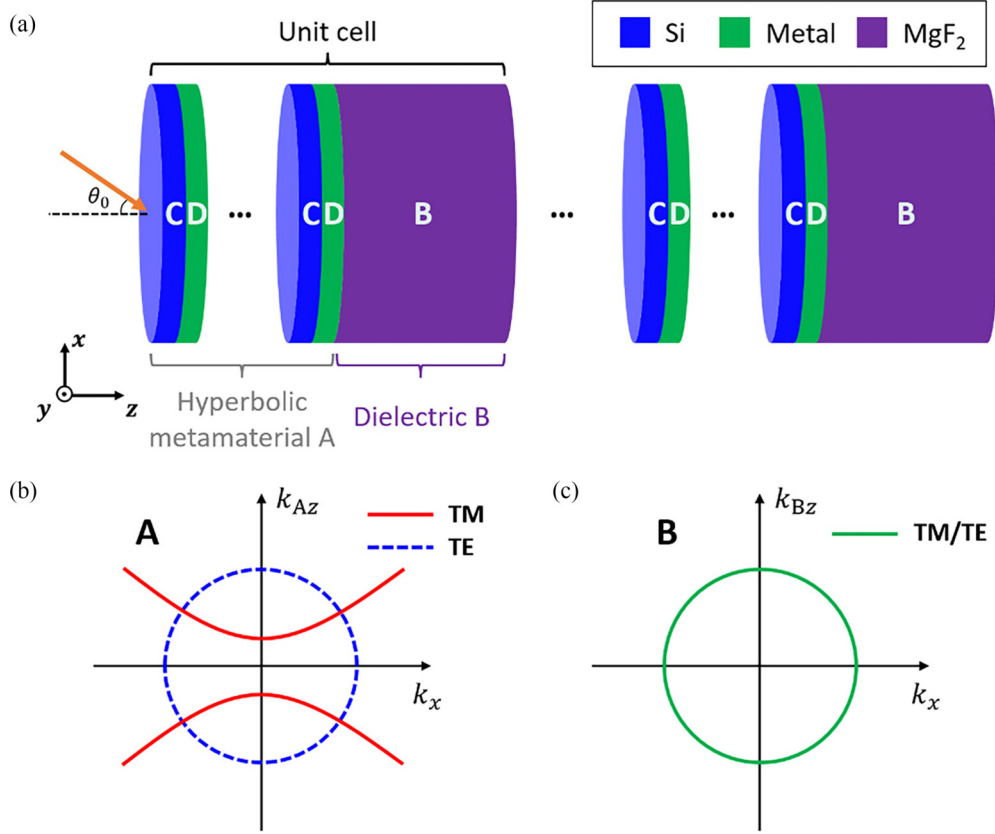


FIG. 12. (a) Schematic of the hybrid 1D PhC composed of alternating hyperbolic metamaterial layers (A layers) and dielectric layers (B layers). The hyperbolic metamaterial layers are mimicked by dielectric-metal subwavelength multilayers (CD)^M. Schematics of the IFCs of (b) hyperbolic metamaterial A and (c) dielectric B under TM and TE polarizations.

In Eq. (17), $n_0 = 1$ denotes the refractive index of the incident medium.

At normal incidence ($\theta_0 = 0^\circ$), we have $\theta_A^{\text{TM}}(0^\circ) = 0^\circ$. Substituting $\theta_A^{\text{TM}}(0^\circ) = 0^\circ$ into Eq. (5), we obtain $n_A^{\text{TM}}(0^\circ) = \sqrt{\varepsilon_{Ax}}$. To close the angle-driven PBG at normal incidence, we set

$$n_A^{\text{TM}}(0^\circ) = \sqrt{\varepsilon_{Ax}} = n_B = 1.37. \quad (18)$$

Combining Eqs. (13a) and (18), the filling ratio of dielectric C can be calculated as

$$p = \frac{\varepsilon_B - \varepsilon_D}{\varepsilon_C - \varepsilon_D} = 0.4019. \quad (19)$$

Then, combining Eqs. (16) and (17), the dependence of the effective refractive index of hyperbolic metamaterial A under TM polarization on the incident angle $n_A^{\text{TM}}(\theta_0)$ can be solved, as shown by the red solid line in Fig. 3. At normal incidence, $n_A^{\text{TM}}(0^\circ) = n_B = 1.37$. Therefore, no PBG is opened due to the lack of the refractive index contrast. At oblique incidence, $n_A^{\text{TM}}(\theta_0) \neq n_B = 1.37$. Therefore, a PBG is opened under TM polarization empowered by the refractive index contrast. As the incident angle increases from 0° to $\sim 90^\circ$, the refractive index contrast gradually increases since n_A^{TM} increases from 1.37 to 1.7433. As a result, the PBG under TM polarization is gradually enlarged. Substituting Eq. (19) into Eqs. (13a) and (13b), we have $\varepsilon_{Ax} = 1.8769 > 0$ and $\varepsilon_{Az} = -11.5701 < 0$.

Hence, the dielectric-metal subwavelength multilayer (CD)⁴⁰⁰ can be treated as a type-I hyperbolic metamaterial.

Under TE polarization, hyperbolic metamaterial A can be treated as an isotropic medium since its IFC is a circle. The effective refractive index of hyperbolic metamaterial n_A^{TE} is independent of the incident angle θ_0 , i.e., [64]

$$n_A^{\text{TE}} = \sqrt{\varepsilon_{Ax}} = 1.37. \quad (20)$$

As shown by the blue dashed line in Fig. 13, $n_A^{\text{TE}} = n_B = 1.37$ is always satisfied at any incident angle. Therefore, no PBG is opened under TE polarization at both normal and oblique incidences.

According to the Bragg scattering theory, the Bragg condition of the first-order angle-driven PBG under TM polarization takes the following form [65]:

$$\begin{aligned} \Phi(\lambda_{\text{Brg}}^{\text{TM}}, \theta_0) &= \Phi_A(\lambda_{\text{Brg}}^{\text{TM}}, \theta_0) + \Phi_B(\lambda_{\text{Brg}}^{\text{TM}}, \theta_0) \\ &= k_{Az}(\lambda_{\text{Brg}}^{\text{TM}}, \theta_0)d_A + k_{Bz}(\lambda_{\text{Brg}}^{\text{TM}}, \theta_0)d_B = \pi, \end{aligned} \quad (21)$$

where Φ denotes the propagating phase in a unit cell of the hybrid 1D PhC, $\lambda_{\text{Brg}}^{\text{TM}}$ denotes the Bragg wavelength of the first-order PBG under TM polarization, d_A denotes the thickness of the hyperbolic metamaterial layer, and d_B denotes the thickness of the dielectric layer.

It is known that the propagating phase in a unit cell of the hybrid 1D PhC under TM polarization can be expressed as a

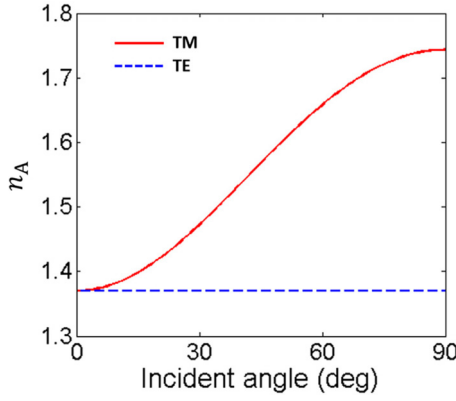


FIG. 13. Dependences of the effective refractive indices of hyperbolic metamaterial A on the incident angle under TM and TE polarizations.

binary function of the wavelength and incident angle, i.e.,

$$\begin{aligned}\Phi(\lambda, \theta_0) &= \Phi_A(\lambda, \theta_0) + \Phi_B(\lambda, \theta_0) \\ &= k_{Az}(\lambda, \theta_0)d_A + k_{Bz}(\lambda, \theta_0)d_B.\end{aligned}\quad (22)$$

To realize a zero-shift angle-driven PBG, the propagating phase in a unit cell of the hybrid 1D PhC under TM polarization must be independent of the incident angle, i.e., $\partial\Phi/\partial\theta_0 = 0$. Since the IFC of hyperbolic metamaterial A under TM polarization is a hyperbola, we have $\partial k_{Az}/\partial\theta_0 > 0$ and $\partial\Phi_A/\partial\theta_0 > 0$. Since the IFC of dielectric B under TM polarization is a circle, we have $\partial k_{Bz}/\partial\theta_0 < 0$ and $\partial\Phi_B/\partial\theta_0 < 0$. Therefore, $\partial\Phi/\partial\theta_0 = 0$ can be achieved when the phase variation of hyperbolic metamaterial layer with respect to the incident angle $\partial\Phi_A/\partial\theta_0$ is compensated with that of dielectric layer with respect to the incident angle $\partial\Phi_B/\partial\theta_0$.

Combining Eqs. (14a), (15), (21), (22), and $\partial\Phi/\partial\theta_0 = 0$, after some algebra [69], the thicknesses of the hyperbolic metamaterial and dielectric layers should satisfy

$$d_A = \frac{\lambda_{\text{Brg}}^{\text{TM}}(0^\circ)}{2} \frac{1}{\sqrt{\varepsilon_{Ax}(1 - \frac{\varepsilon_B}{\varepsilon_{Az}})}}, \quad (22a)$$

$$d_B = \frac{\lambda_{\text{Brg}}^{\text{TM}}(0^\circ)}{2} \frac{1}{\sqrt{\varepsilon_B(1 - \frac{\varepsilon_{Az}}{\varepsilon_B})}}, \quad (22b)$$

where $\lambda_{\text{Brg}}^{\text{TM}}(0^\circ)$ denotes the Bragg wavelength of the first-order PBG at normal incidence under TM polarization.

Substituting Eqs. (14a) and (15) into Eq. (21), we can obtain the solution of Eq. (21), i.e.,

$$\lambda_{\text{Brg}}^{\text{TM}}(\theta_0) = 2 \left(\sqrt{\varepsilon_{Ax} - \frac{\varepsilon_{Ax}}{\varepsilon_{Az}} \sin^2 \theta_0} d_A + \sqrt{\varepsilon_B - \sin^2 \theta_0} d_B \right). \quad (23)$$

When Eqs. (22a) and (22b) are satisfied, the Bragg wavelength of the first-order PBG under TM polarization $\lambda_{\text{Brg}}^{\text{TM}}$ is insensitive to the incident angle θ_0 . Therefore, the position of the angle-driven PBG under TM polarization keeps almost unshifted.

In our design, the Bragg wavelength of the first-order angle-driven PBG at normal incidence is set to be $\lambda_{\text{Brg}}^{\text{TM}}(0^\circ) = 1500$ nm. Substituting $\lambda_{\text{Brg}}^{\text{TM}}(0^\circ) = 1500$ nm into

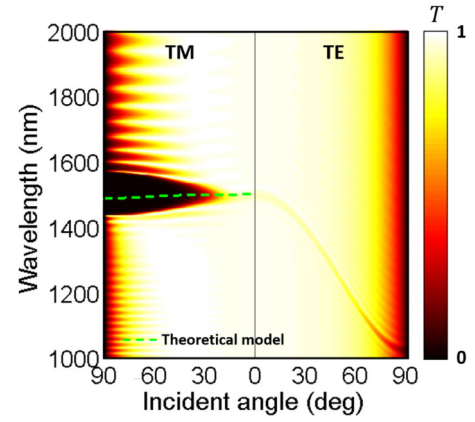


FIG. 14. Dependence of the transmittance spectrum of the hybrid 1D PhC $[(\text{CD})^{400}\text{B}]^{40}$ on the incident angle under TM and TE polarizations. Green dashed line represents the dependence of the Bragg wavelength predicted by the theoretical model on the incident angle.

Eqs. (22a) and (22b), the thicknesses of the hyperbolic metamaterial and dielectric layers can be obtained, i.e., $d_A = 471.03$ nm and $d_B = 76.41$ nm. To ensure the accuracy of the EMA, the number of periods in hyperbolic metamaterial layer is chosen to be $M = 400$. Since $p = 0.4019$, the thicknesses of C and D layers in the hyperbolic metamaterial layer can be calculated as $d_C = pd_A/400 = 0.473$ nm and $d_D = (1-p)d_A/400 = 0.704$ nm, respectively. The thickness of a unit cell in the hyperbolic metamaterial layer is only $d_{A,\text{Unit}} = d_C + d_D = 1.177$ nm $\approx 0.00078\lambda_{\text{Brg}}^{\text{TM}}(0^\circ)$, indicates that the deep subwavelength condition is satisfied.

To realize a deep angle-driven PBG, the number of periods in the hybrid 1D PhC is chosen to be $N = 40$. According to the transfer matrix method [64], we numerically calculate the dependence of the transmittance spectrum of the hybrid 1D PhC $[(\text{CD})^{400}\text{B}]^{40}$ on the incident angle under TM and TE polarizations, as depicted in Fig. 14. As demonstrated, a zero-shift angle-driven PBG occurs. Under TM polarization, the angle-driven PBG is closed at normal incidence while it is opened at oblique incidence. The position of the angle-driven PBG is insensitive to the incident angle. Under TE polarization, the angle-driven PBG keeps closed at both normal and oblique incidences. Also, we calculate the dependence of the Bragg wavelength predicted by the theoretical model [Eq. (23)] on the incident angle, as shown in the green dashed line. As demonstrated, the theoretical model agrees well with the numerical results.

Figure 15(a) gives the transmittance spectra of the hybrid 1D PhC $[(\text{CD})^{400}\text{B}]^{40}$ under TM polarization at different incident angles $\theta_0 = 0^\circ, 30^\circ, 50^\circ$, and 70° . Clearly, the angle-driven PBG is closed at normal incidence while is opened at oblique incidence. Also, the position of the angle-driven PBG is insensitive to the incident angle. For $\theta_0 = 30^\circ, 50^\circ$, and 70° , the angle-driven PBG is opened around 1500 nm. Figure 15(b) gives the transmittance spectra of the hybrid 1D PhC $[(\text{CD})^{400}\text{B}]^{40}$ under TE polarization at different incident angles $\theta_0 = 0^\circ, 30^\circ, 50^\circ$, and 70° . Clearly, the angle-driven PBG is closed at both normal and oblique incidences. Therefore, the angle-driven PBG exhibits a superior polarization-dependent

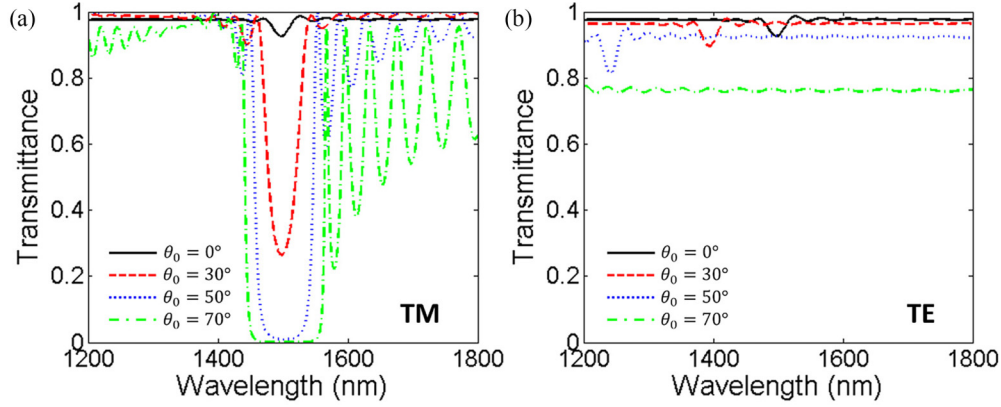


FIG. 15. (a) Transmittance spectra of the hybrid 1D PhC [(CD)⁴⁰⁰B]⁴⁰ under TM polarization at different incident angles $\theta_0 = 0^\circ, 30^\circ, 50^\circ$, and 70° . (b) Transmittance spectra of the hybrid 1D PhC [(CD)⁴⁰⁰B]⁴⁰ under TE polarization at different incident angles $\theta_0 = 0^\circ, 30^\circ, 50^\circ$, and 70° .

property. Empowered by the superior polarization-dependent and zero-shift properties of the zero-shift angle-driven PBG, wide-angle polarization selection can be achieved.

B. Wide-angle polarization selection empowered by zero-shift angle-driven PBGs

In this subsection, we utilize the superior polarization-dependent and zero-shift properties of the zero-shift angle-driven PBG to achieve wide-angle polarization selection. The materials and thicknesses of the hybrid 1D PhC are the same as those in Sec. III A. The incident and exit media are air with a relative permittivity $\epsilon_0 = n_0^2 = 1^2$ and MgF₂ with a relative permittivity $\epsilon_S = n_S^2 = 1.37^2$ [62], respectively.

Figure 16(a) gives the transmittance angular spectra of the hybrid 1D PhC [(CD)⁴⁰⁰B]⁴⁰ under TM and TE polarizations at $\lambda = 1500$ nm. At normal incidence, the transmittance is high (0.927) since the angle-driven PBG is closed. As the incident angle increases, the transmittance under TM polarization decreases rapidly since the angle-driven PBG is opened. However, the transmittance under TE polarization decreases slowly since the angle-driven PBG is closed. Figure 16(b) gives the polarization selection ratio angular spectrum of the hybrid 1D PhC [(CD)⁴⁰⁰B]⁴⁰ at $\lambda = 1500$ nm. As the incident

increases from 0° to $\sim 90^\circ$, the polarization selection ratio rapidly increases from 1.00×10^0 to 1.42×10^4 . We define the angle range where the polarization selection ratio is higher than 10^2 as the operating angle range. The operating angle range is from 49.86° to $\sim 90^\circ$. The width of the operating angle range reaches 40.14° .

C. Zero-shift angle-driven TPPs in heterostructures consisting of a metal layer and a hybrid 1D PhC containing hyperbolic metamaterials

In this subsection, we realize a zero-shift angle-driven TPP in a heterostructure consisting of a metal layer and a hybrid 1D PhC containing hyperbolic metamaterials with a zero-shift angle-driven PBG. Figure 17(a) depicts the schematic of the proposed heterostructure. The whole heterostructure can be represented as $M[(CD)^M B]^N$. The material of M layer is selected to be ITO [68]. The relative permittivity of ITO can be described by the Drude model, i.e., $\epsilon_M = \epsilon_{M,\text{inf}} - \omega_{M,p}^2 / (\omega^2 + i\gamma_M\omega)$, where $\epsilon_{M,\text{inf}} = 3.9$ denotes the high-frequency relative permittivity, $\hbar\omega_{M,p} = 2.48$ eV denotes the plasma energy, and $\hbar\gamma_M = 0.016$ eV denotes the damping energy [68]. The materials and thicknesses of the hybrid 1D PhC are the same as those in Sec. III A. The incident

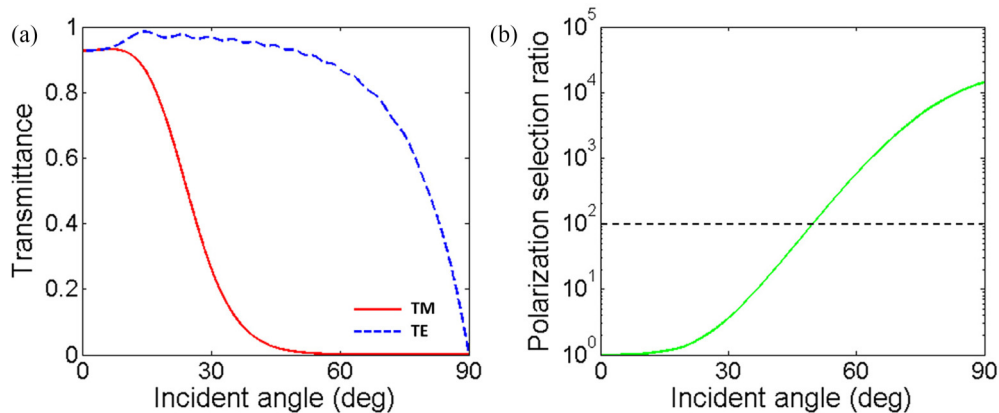


FIG. 16. (a) Transmittance angular spectra of the hybrid 1D PhC [(CD)⁴⁰⁰B]⁴⁰ under TM and TE polarizations at $\lambda = 1500$ nm. (b) Polarization selection ratio angular spectrum of the hybrid 1D PhC [(CD)⁴⁰⁰B]⁴⁰ at $\lambda = 1500$ nm. The black dashed line represents the polarization selection ratio equal to 10^2 .

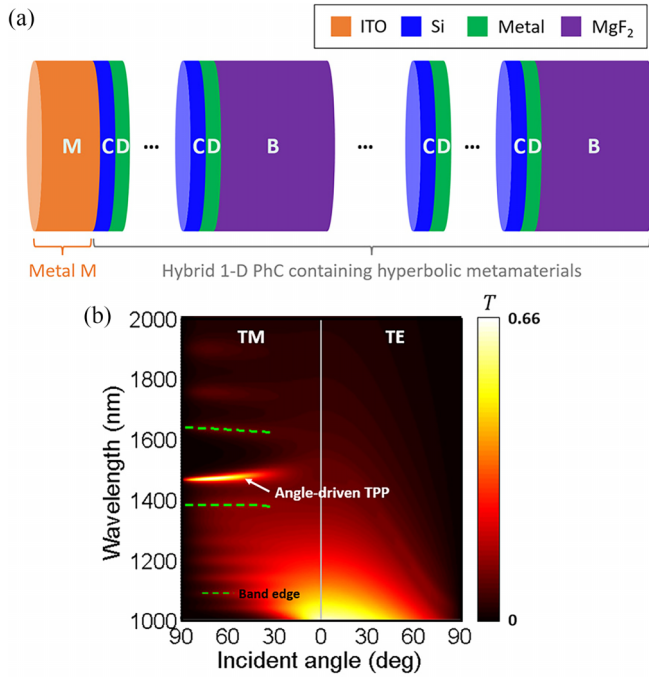


FIG. 17. (a) Schematic of the heterostructure consisting of a metal layer (M layer) and a hybrid 1D PhC composed of alternating hyperbolic metamaterial layers (A layers) and dielectric layers (B layers). (b) Dependence of the transmittance spectrum of the heterostructure $M[(CD)^{400}B]^{15}$ on the incident angle under TM and TE polarizations. Green dashed lines represent the dependences of the wavelengths of two band edges on the incident angle.

and exit media are air with a relative permittivity $\epsilon_0 = n_0^2 = 1^2$ and MgF_2 with a relative permittivity $\epsilon_S = n_S^2 = 1.37^2$ [62], respectively.

Now, we design the heterostructure to realize a zero-shift angle-driven TPP. The thickness of M layer is set to be $d_M = 180$ nm. To realize a zero-shift angle-driven TPP, a wide zero-shift angle-driven PBG is required. Hence, the number of periods in the hybrid 1D PhC is chosen to be $N = 15$. According to the transfer matrix method [64], we numerically calculate the dependence of the transmittance spectrum of the

heterostructure $M[(CD)^{400}B]^{15}$ on the incident angle under TM and TE polarizations, as depicted in Fig. 17(b). The green dashed lines represent the dependences of the wavelengths of two band edges on the incident angle. As demonstrated, a zero-shift angle-driven TPP occurs. Under TM polarization, the angle-driven TPP does not occur at normal incidence. As the incident angle increases to 30° , the angle-driven TPP occurs at 1479.86 nm. As the incident angle continues to increase to $\sim 90^\circ$, the angle-driven TPP slightly shifts to 1461.94 nm. The relative shift of the angle-driven TPP is only 1.21%. Under TE polarization, the angle-driven TPP does not occur at both normal and oblique incidences.

Figure 18(a) gives the transmittance spectra of the heterostructure $M[(CD)^{400}B]^{15}$ under TM polarization at different incident angles $\theta_0 = 0^\circ, 30^\circ, 50^\circ$, and 70° . Clearly, the angle-driven TPP does not occur at normal incidence while it does occur at oblique incidence. Also, the position of the angle-driven TPP is insensitive to the incident angle. Figure 18(b) gives the transmittance spectra of the heterostructure $M[(CD)^{400}B]^{15}$ under TE polarization at different incident angles $\theta_0 = 0^\circ, 30^\circ, 50^\circ$, and 70° . Clearly, the angle-driven TPP does not occur at both normal and oblique incidences. Therefore, the angle-driven TPP exhibits a superior polarization-dependent property. Empowered by the superior polarization-dependent and zero-shift properties of the zero-shift angle-driven TPP, wide-angle polarization selection can be achieved.

IV. CONCLUSIONS

In summary, we realize blueshift and zero-shift angle-driven PBGs in hybrid 1D PhCs composed of alternating anisotropic metamaterial and dielectric layers. Under TM polarization, the angle-driven PBG is closed at normal incidence while is opened at oblique incidence. Under TE polarization, the angle-driven PBG is closed at both normal and oblique incidences. In hybrid 1D PhCs composed of alternating elliptical metamaterial and dielectric layers, we realize blueshift angle-driven PBGs under TM polarization. Assisted by the blueshift angle-driven PBG, broadband polarization selection and privacy protection can be achieved. In hybrid 1D PhCs

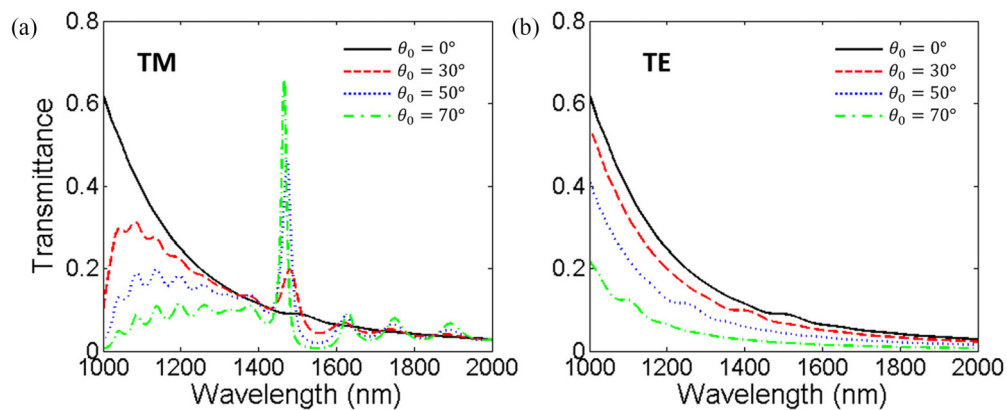


FIG. 18. (a) Transmittance spectra of the heterostructure $M[(CD)^{400}B]^{15}$ under TM polarization at different incident angles $\theta_0 = 0^\circ, 30^\circ, 50^\circ$, and 70° . (b) Transmittance spectra of the heterostructure $M[(CD)^{400}B]^{15}$ under TE polarization at different incident angles $\theta_0 = 0^\circ, 30^\circ, 50^\circ$, and 70° .

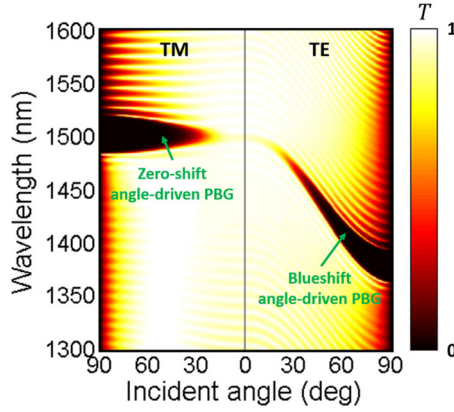


FIG. 19. Dependence of the transmittance spectrum of the hybrid 1D PhC $[(\text{CD})^{400}\text{B}]^{40}$ on the incident angle under TM and TE polarizations. The dispersion of the metal is considered.

composed of alternating hyperbolic metamaterial and dielectric layers, we realize zero-shift angle-driven PBGs under TM polarization. Assisted by the zero-shift angle-driven PBG, wide-angle polarization selection can be achieved. By placing a metal layer in front of the hybrid 1D PhCs to constitute the heterostructures, blueshift and zero-shift angle-driven TPPs can be realized. Our work provides a viable route to realizing angle-driven PBGs and angle-driven TPPs.

ACKNOWLEDGMENTS

This work is sponsored by the National Natural Science Foundation of China (Grant No. 12104105), the Guangdong Basic and Applied Basic Research Foundation (Grant No. 2023A1515011024), and the Start-up Funding of Guangdong Polytechnic Normal University (Grant No. 2021SDKYA033).

APPENDIX: EFFECTS OF DISPERSION AND LOSS OF METAL ON ZERO-SHIFT ANGLE-DRIVEN PBGS AND ZERO-SHIFT ANGLE-DRIVEN TPPS

Here, we investigate the effects of the dispersion and loss of the metal on the zero-shift angle-driven PBG and zero-shift

angle-driven TPP. The material of the D layer is selected to be a dispersive metal with a relative permittivity described by the Drude model, i.e., $\varepsilon_D = \varepsilon_{D,\text{inf}} - \omega_{D,p}^2 / (\omega^2 + i\gamma_D\omega)$, where $\varepsilon_{D,\text{inf}}$ denotes the high-frequency relative permittivity, $\hbar\omega_{D,p}$ denotes the plasma energy, and $\hbar\gamma_D$ denotes the damping energy. The materials of C and D layers are the same as those in Sec. III. Also, the incident and exit media are the same as those in Sec. III.

Initially, we consider the dispersion and ignore the loss, i.e., $\hbar\gamma_D = 0$. The high-frequency relative permittivity and plasma energy are taken from a kind of infrared plasmonic materials, ITO, i.e., $\varepsilon_{D,\text{inf}} = 3.9$ and $\hbar\omega_{D,p} = 2.48$ eV [68]. The Bragg wavelength of the first-order angle-driven PBG at normal incidence is set to be $\lambda_{\text{Brg}}^{\text{TM}}(0^\circ) = 1500$ nm. According to Eq. (19), the filling ratio of dielectric C can be calculated as $p = 0.4042$. Substituting $\lambda_{\text{Brg}}^{\text{TM}}(0^\circ) = 1500$ nm into Eqs. (22a) and (22b), the thicknesses of the hyperbolic metamaterial and dielectric layers can be obtained, i.e., $d_A = 472.71$ nm and $d_B = 74.74$ nm. To ensure the accuracy of the EMA, the number of periods in hyperbolic metamaterial layer is chosen to be $M = 400$. Since $p = 0.4042$, the thicknesses of C and D layers in the hyperbolic metamaterial layer can be calculated as $d_C = pd_A/400 = 0.478$ nm and $d_D = (1-p)d_A/400 = 0.704$ nm, respectively. The thickness of a unit cell in the hyperbolic metamaterial layer is only $d_{A,\text{Unit}} = d_C + d_D = 1.182$ nm $\approx 0.00079\lambda_{\text{Brg}}^{\text{TM}}(0^\circ)$, which indicates that the deep subwavelength condition is satisfied.

To realize a deep angle-driven PBG, the number of periods in the hybrid 1D PhC is chosen to be $N = 40$. According to the transfer matrix method [64], we numerically calculate the dependence of the transmittance spectrum of the hybrid 1D PhC $[(\text{CD})^{400}\text{B}]^{40}$ on the incident angle under TM and TE polarizations, as depicted in Fig. 19. Under TM polarization, a zero-shift angle-driven PBG still occurs when considering the dispersion of the metal.

Interestingly, an extra blueshift angle-driven PBG occurs under TE polarization when considering the dispersion of the metal. In the following, we explain the formation of this blueshift angle-driven PBG. According to the Bragg scattering theory, the Bragg condition of the first-order angle-driven

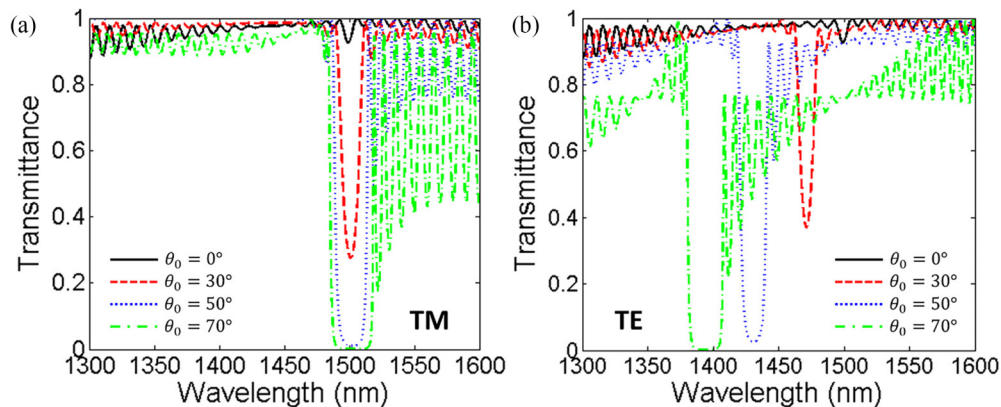


FIG. 20. (a) Transmittance spectra of the hybrid 1D PhC $[(\text{CD})^{400}\text{B}]^{40}$ under TM polarization at different incident angles $\theta_0 = 0^\circ, 30^\circ, 50^\circ$, and 70° . (b) Transmittance spectra of the hybrid 1D PhC $[(\text{CD})^{400}\text{B}]^{40}$ under TE polarization at different incident angles $\theta_0 = 0^\circ, 30^\circ, 50^\circ$, and 70° . The dispersion of the metal is considered.

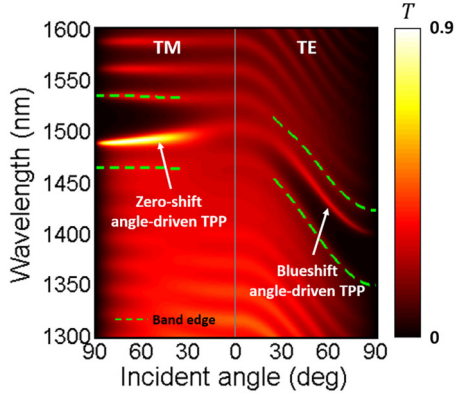


FIG. 21. Dependence of the transmittance spectrum of the heterostructure $M[(\text{CD})^{400}\text{B}]^{15}$ on the incident angle under TM and TE polarizations. Green dashed lines represent the dependences of the wavelengths of four band edges on the incident angle. The dispersion of the metal is considered.

PBG under TE polarization takes the following form [65]:

$$\begin{aligned}\Phi(\lambda_{\text{Brg}}^{\text{TE}}, \theta_0) &= \Phi_A(\lambda_{\text{Brg}}^{\text{TE}}, \theta_0) + \Phi_B(\lambda_{\text{Brg}}^{\text{TE}}, \theta_0) \\ &= k_{A_z}(\lambda_{\text{Brg}}^{\text{TE}}, \theta_0)d_A + k_{B_z}(\lambda_{\text{Brg}}^{\text{TE}}, \theta_0)d_B = \pi, \quad (\text{A1})\end{aligned}$$

where Φ denotes the propagating phase in a unit cell of the hybrid 1D PhC, $\lambda_{\text{Brg}}^{\text{TE}}$ denotes the Bragg wavelength of the first-order PBG under TE polarization, d_A denotes the thickness of the hyperbolic metamaterial layer, and d_B denotes the thickness of the dielectric layer.

Substituting Eqs. (14b) and (15) into Eq. (A1), we can obtain the solution of Eq. (A1), i.e.,

$$\lambda_{\text{Brg}}^{\text{TE}}(\theta_0) = 2(\sqrt{\varepsilon_{A_x} - \sin^2\theta_0}d_A + \sqrt{\varepsilon_B - \sin^2\theta_0}d_B). \quad (\text{A2})$$

According to Eq. (A2), the Bragg wavelength of the first-order PBG under TE polarization $\lambda_{\text{Brg}}^{\text{TE}}$ decreases as the incident angle θ_0 increases. At normal incidence ($\theta_0 = 0^\circ$), the PBG is closed since $n_A^{\text{TE}}[\lambda_{\text{Brg}}^{\text{TE}}(0^\circ)] = \sqrt{\varepsilon_{A_x}[\lambda_{\text{Brg}}^{\text{TE}}(0^\circ)]} = n_B = 1.37$. Nevertheless, at oblique incidence ($\theta_0 \neq 0^\circ$), the Bragg wavelength of the first-order PBG under TE

polarization $\lambda_{\text{Brg}}^{\text{TE}}$ decreases. Since metal D is dispersive, the hyperbolic metamaterial (A layer) is also dispersive. At oblique incidence ($\theta_0 \neq 0^\circ$), we have $n_A^{\text{TE}}[\lambda_{\text{Brg}}^{\text{TE}}(\theta_0)] = \sqrt{\varepsilon_{A_x}[\lambda_{\text{Brg}}^{\text{TE}}(\theta_0)]} \neq n_B$. Owing to the refractive index contrast between the hyperbolic metamaterial and dielectric layers, a PBG occurs under TE polarization.

Figure 20(a) gives the transmittance spectra of the hybrid 1D PhC $[(\text{CD})^{400}\text{B}]^{40}$ under TM polarization at different incident angles $\theta_0 = 0^\circ, 30^\circ, 50^\circ$, and 70° . Clearly, the angle-driven PBG is closed at normal incidence while it is opened at oblique incidence. Also, the position of the angle-driven PBG is insensitive to the incident angle. For $\theta_0 = 30^\circ, 50^\circ$, and 70° , the angle-driven PBG is opened around 1500 nm. Figure 20(b) gives the transmittance spectra of the hybrid 1D PhC $[(\text{CD})^{400}\text{B}]^{40}$ under TE polarization at different incident angles $\theta_0 = 0^\circ, 30^\circ, 50^\circ$, and 70° . Clearly, the angle-driven PBG is closed at normal incidence while is opened at oblique incidence. As the incident angle increases, the angle-driven PBG strongly shifts towards shorter wavelengths.

To realize angle-driven TPPs under TM and TE polarizations, we placed an ITO layer in front of the hybrid 1D PhCs. The relative permittivity of ITO can be described by the Drude model, i.e., $\varepsilon_M = \varepsilon_{M,\text{inf}} - \omega_{M,p}^2/(\omega^2 + i\gamma_M\omega)$, where $\varepsilon_{M,\text{inf}} = 3.9$ denotes the high-frequency relative permittivity, $\hbar\omega_{M,p} = 2.48$ eV denotes the plasma energy, and $\hbar\gamma_M = 0.016$ eV denotes the damping energy [68]. The whole heterostructure can be represented as $M[(\text{CD})^{400}\text{B}]^{15}$. The incident and exit media are air with a relative permittivity $\varepsilon_0 = n_0^2 = 1^2$ and MgF_2 with a relative permittivity $\varepsilon_S = n_S^2 = 1.37^2$ [62], respectively. To realize angle-driven TPPs under TM and TE polarizations, the thickness of the M layer is set to be $d_M = 120$ nm. According to the transfer matrix method [64], we numerically calculate the dependence of the transmittance spectrum of the heterostructure $M[(\text{CD})^{400}\text{B}]^{15}$ on the incident angle under TM and TE polarizations, as depicted in Fig. 21. The green dashed lines represent the dependences of the wavelengths of four band edges on the incident angle. As demonstrated, a zero-shift angle-driven TPP occurs under TM polarization while a blueshift angle-driven TPP occurs under

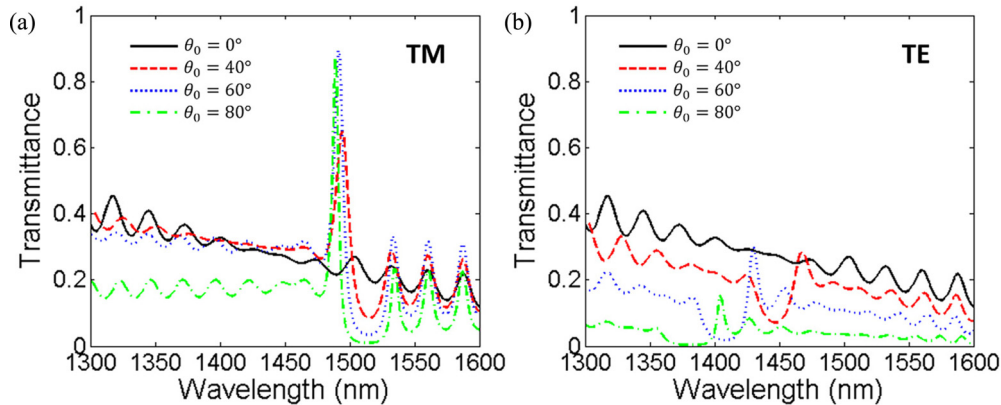


FIG. 22. (a) Transmittance spectra of the heterostructure $M[(\text{CD})^{400}\text{B}]^{15}$ under TM polarization at different incident angles $\theta_0 = 0^\circ, 30^\circ, 50^\circ$, and 70° . (b) Transmittance spectra of the heterostructure $M[(\text{CD})^{400}\text{B}]^{15}$ under TE polarization at different incident angles $\theta_0 = 0^\circ, 30^\circ, 50^\circ$, and 70° . The dispersion of the metal is considered.

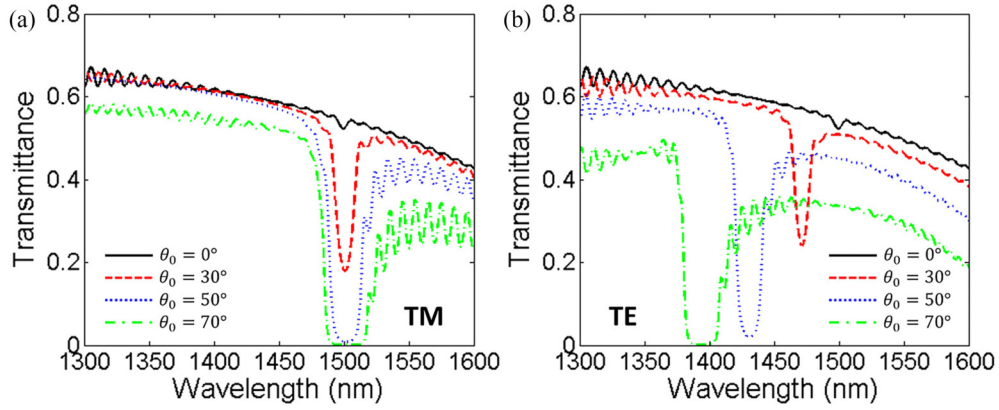


FIG. 23. (a) Transmittance spectra of the hybrid 1D PhC $[(\text{CD})^{400} \text{B}]^{40}$ under TM polarization at different incident angles $\theta_0 = 0^\circ, 30^\circ, 50^\circ$, and 70° . (b) Transmittance spectra of the hybrid 1D PhC $[(\text{CD})^{400} \text{B}]^{40}$ under TE polarization at different incident angles $\theta_0 = 0^\circ, 30^\circ, 50^\circ$, and 70° . Both the dispersion and loss of the metal are considered.

TE polarization. Under TM polarization, the angle-driven TPP does not occur at normal incidence. As the incident angle increases to 32° , the angle-driven TPP occurs at 1495.53 nm. As the incident angle continues to increase to $\sim 90^\circ$, the angle-driven TPP slightly shifts to 1488.72 nm. The relative shift of the angle-driven TPP is only 0.46%. Under TE polarization, the angle-driven TPP does not occur at normal incidence. As the incident angle increases to 20° , the angle-driven TPP occurs at 1495.73 nm. As the incident angle continues to increase to $\sim 90^\circ$, the angle-driven TPP strongly shifts to 1401.11 nm. The relative shift of the angle-driven TPP reaches 6.33%.

Figure 22(a) gives the transmittance spectra of the heterostructure $\text{M}[(\text{CD})^{400} \text{B}]^{15}$ under TM polarization at different incident angles $\theta_0 = 0^\circ, 40^\circ, 60^\circ$, and 80° . Clearly, the angle-driven TPP does not occur at normal incidence while occurs at oblique incidence. Also, the position of the angle-driven TPP is insensitive to the incident angle. Figure 22(b) gives the transmittance spectra of the heterostructure $\text{M}[(\text{CD})^{400} \text{B}]^{15}$ under TE polarization at different incident angles $\theta_0 = 0^\circ, 40^\circ, 60^\circ$, and 80° . Clearly, the angle-driven TPP does not occur at normal incidence

while occurs at oblique incidence. As the incident angle increases, the angle-driven TPP strongly shifts towards shorter wavelengths.

Now, we consider the dispersion and loss of the metal (D layer) simultaneously. The damping energy of the metal is set to be 1/10 times of the damping energy of ITO, i.e., $\hbar\gamma_D = 0.0016$ eV. Figure 23(a) gives the transmittance spectra of the hybrid 1D PhC $[(\text{CD})^{400} \text{B}]^{40}$ under TM polarization at different incident angles $\theta_0 = 0^\circ, 30^\circ, 50^\circ$, and 70° . Compared with Fig. 20(a), the transmittance is reduced due to the loss of the metal layers. The angle-driven PBG is closed at normal incidence while it is opened at oblique incidence. Also, the position of the angle-driven PBG is insensitive to the incident angle. For $\theta_0 = 30^\circ, 50^\circ$, and 70° , the angle-driven PBG is opened around 1500 nm. Figure 23(b) gives the transmittance spectra of the hybrid 1D PhC $[(\text{CD})^{400} \text{B}]^{40}$ under TE polarization at different incident angles $\theta_0 = 0^\circ, 30^\circ, 50^\circ$, and 70° . Compared with Fig. 20(b), the transmittance is reduced due to the loss of the metal layers. The angle-driven PBG is closed at normal incidence while is opened at oblique incidence. As the incident angle increases, the angle-driven PBG strongly shifts towards shorter wavelengths.

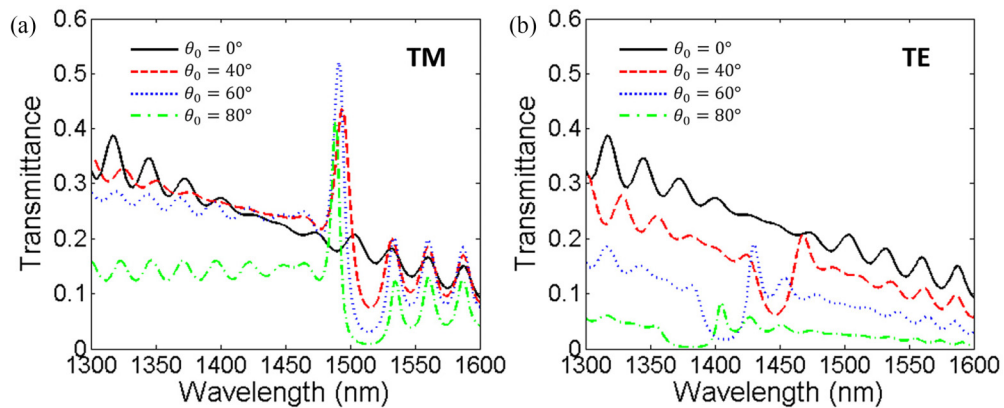


FIG. 24. (a) Transmittance spectra of the heterostructure $\text{M}[(\text{CD})^{400} \text{B}]^{15}$ under TM polarization at different incident angles $\theta_0 = 0^\circ, 40^\circ, 60^\circ$, and 80° . (b) Transmittance spectra of the heterostructure $\text{M}[(\text{CD})^{400} \text{B}]^{15}$ under TE polarization at different incident angles $\theta_0 = 0^\circ, 40^\circ, 60^\circ$, and 80° . Both the dispersion and loss of the metal are considered.

Figure 24(a) gives the transmittance spectra of the heterostructure $M[(CD)^{400}B]^{15}$ under TM polarization at different incident angles $\theta_0 = 0^\circ, 40^\circ, 60^\circ,$ and 80° . Compared with Fig. 22(a), the transmittance is reduced due to the loss of the metal layers. The angle-driven TPP does not occur at normal incidence while it does occur at oblique incidence. Also, the position of the angle-driven TPP is insensitive to the incident angle. Figure 24(b) gives the

transmittance spectra of the heterostructure $M[(CD)^{400}B]^{15}$ under TE polarization at different incident angles $\theta_0 = 0^\circ, 40^\circ, 60^\circ,$ and 80° . Compared with Fig. 22(b), the transmittance is reduced due to the loss of the metal layers. The angle-driven TPP does not occur at normal incidence while occurs at oblique incidence. As the incident angle increases, the angle-driven TPP strongly shifts towards shorter wavelengths.

-
- [1] E. Yablonovitch, Inhibited spontaneous emission in solid-state physics and electronics, *Phys. Rev. Lett.* **58**, 2059 (1987).
- [2] S. John, Strong localization of photons in certain disordered dielectric superlattices, *Phys. Rev. Lett.* **58**, 2486 (1987).
- [3] J. D. Joannopoulos, P. R. Villeneuve, and S. Fan, Photonic crystals, *Solid State Commun.* **102**, 165 (1997).
- [4] M. Kalitkevski, I. Iorsh, S. Brand, R. A. Abram, J. M. Chamberlain, A. V. Kavokin, and I. A. Shelykh, Tamm plasmon-polaritons: Possible electromagnetic states at the interface of a metal and a dielectric Bragg mirror, *Phys. Rev. B* **76**, 165415 (2007).
- [5] F. Wu, X. Wu, S. Xiao, G. Liu, and H. Li, Broadband wide-angle multilayer absorber based on a broadband omnidirectional optical Tamm state, *Opt. Express* **29**, 23976 (2021).
- [6] J. Wu, F. Wu, T. Zhao, M. Antezza, and X. Wu, Dual-band non-reciprocal thermal radiation by coupling optical Tamm states in magnetophotonic multilayers, *Int. J. Therm. Sci.* **175**, 107457 (2022).
- [7] A. Angelini, E. Enrico, E. De Leo, P. Munzert, L. Boarino, F. Michelotti, F. Giorgis, and E. Descrovi, Fluorescence diffraction assisted by Bloch surface waves on a one-dimensional photonic crystal, *New J. Phys.* **15**, 073002 (2013).
- [8] R. Kanok, M. Abuleil, P. Hlubina, and I. Abdulhalim, Bloch surface wave fast ellipsometric sensor utilizing a polarization camera with an improved detection limit, *Opt. Laser Technol.* **179**, 111218 (2024).
- [9] R. K. Lee, O. J. Painter, B. D'Urso, A. Scherer, and A. Yariv, Measurement of spontaneous emission from a two-dimensional photonic band gap defined microcavity at near-infrared wavelengths, *Appl. Phys. Lett.* **74**, 1522 (1999).
- [10] Z.-Y. Li, L.-L. Lin, and Z.-Q. Zhang, Spontaneous emission from photonic crystals: Full vectorial calculations, *Phys. Rev. Lett.* **84**, 4341 (2000).
- [11] Y.-S. Zhou, X.-H. Wang, B.-Y. Gu, and F.-H. Wang, Switching control of spontaneous emission by polarized atoms in two-dimensional photonic crystals, *Phys. Rev. Lett.* **96**, 103601 (2006).
- [12] I. V. Soboleva, V. V. Moskalenko, and A. A. Fedyanin, Giant Goos-Hänchen effect and Fano resonance at photonic crystal surfaces, *Phys. Rev. Lett.* **108**, 123901 (2012).
- [13] I. V. Timofeev, D. N. Maksimov, and A. F. Sadreev, Optical defect mode with tunable Q factor in a one-dimensional anisotropic photonic crystal, *Phys. Rev. B* **97**, 024306 (2018).
- [14] P. S. Pankin, B.-R. Wu, J.-H. Yang, K.-P. Chen, I. V. Timofeev, and A. F. Sadreev, One-dimensional photonic bound states in the continuum, *Commun. Phys.* **3**, 91 (2020).
- [15] Y. Fink, J. N. Winn, S. Fan, C. Chen, J. Michel, J. D. Joannopoulos, and E. L. Thomas, A dielectric omnidirectional reflector, *Science* **282**, 1679 (1998).
- [16] T. A. Birks, J. C. Knight, and P. St. J. Russell, Endlessly single-mode photonic crystal fiber, *Opt. Lett.* **22**, 961 (1997).
- [17] C. Markos, J. C. Travers, A. Abdolvand, B. J. Eggleton, and O. Bang, Hybrid photonic-crystal fiber, *Rev. Mod. Phys.* **89**, 045003 (2017).
- [18] S. Noda, M. Yokoyama, M. Imada, A. Chutinan, and M. Mochizuki, Polarization mode control of two-dimensional photonic crystal laser by unit cell structure design, *Science* **293**, 1123 (2001).
- [19] H.-G. Park, S.-H. Kim, S.-H. Kwon, Y.-G. Ju, J.-K. Yang, J.-H. Baek, S.-B. Kim, and Y.-H. Lee, Electrically driven single-cell photonic crystal laser, *Science* **305**, 1444 (2024).
- [20] X. Wang, Y. Liang, L. Wu, J. Guo, X. Dai, and Y. Xiang, Multi-channel perfect absorber based on a one-dimensional topological photonic crystal heterostructure with graphene, *Opt. Lett.* **43**, 4256 (2018).
- [21] R. G. Bikbaev, S. Ya. Vetrov, and I. V. Timofeev, Hyperbolic metamaterial for the Tamm plasmon polariton application, *J. Opt. Soc. Am. B* **37**, 2215 (2020).
- [22] S. Jena, R. B. Tokas, S. Thakur, and D. V. Udupa, Rabi-like splitting and refractive index sensing with hybrid Tamm plasmon-cavity modes, *J. Phys. D* **55**, 175104 (2022).
- [23] B.-F. Wang, H.-N. Ye, and H.-F. Zhang, Pattern-free tunable angular propagation characteristics based on edge states and its potential in sensing, *IEEE Trans. Antenn. Propag.* **71**, 8949 (2023).
- [24] E. Moggi, G. Pellegrini, J. Gil-Rostra, F. Yubero, G. Simone, S. Fossati, J. Dostálek, R. M. Vázquez, R. Osellame, M. Celebrano, M. Finazzi, and P. Biagioni, One-dimensional photonic crystal for surface mode polarization control, *Adv. Opt. Mater.* **10**, 2200759 (2022).
- [25] F. Wu, T. Liu, and S. Xiao, Polarization-sensitive photonic bandgaps in hybrid one-dimensional photonic crystals composed of all-dielectric elliptical metamaterials and isotropic dielectrics, *Appl. Opt.* **62**, 706 (2023).
- [26] Y. She, D. Liu, J. Li, M. Yao, Y. Zheng, and F. Wu, Tunable wide-angle high-efficiency polarization selectivity based on a one-dimensional photonic crystal containing elliptical metamaterials, *Phys. Lett. A* **494**, 129299 (2024).
- [27] S. Li, G. Feng, Y. Liu, M. Wu, X. Zhao, F. Sun, Z. Gan, Z. Chen, and Y. Yang, Omnidirectional near-infrared narrowband filters based on defective mirror-symmetry one-dimensional photonic crystals containing hyperbolic metamaterials, *Opt. Laser Eng.* **176**, 108107 (2024).

- [28] C. M. Aderson and K. P. Giapis, Larger two-dimensional photonic band gaps, *Phys. Rev. Lett.* **77**, 2949 (1996).
- [29] C.-S. Kee, J.-E. Kim, and H. Y. Park, Absolute photonic band gap in a two-dimensional square lattice dielectric rods in air, *Phys. Rev. E* **56**, R6291(R) (1997).
- [30] Y. Yang, Z. Gao, H. Xue, L. Zhang, M. He, Z. Yang, R. Singh, Y. Chong, B. Zhang, and H. Chen, Realization of a three-dimensional photonic topological insulator, *Nature (London)* **565**, 622 (2019).
- [31] G.-G. Liu, Z. Gao, Q. Wang, X. Xi, Y.-H. Hu, M. Wang, C. Liu, X. Lin, L. Deng, S. A. Yang, P. Zhou, Y. Yang, Y. Chong, and B. Zhang, Topological Chern vectors in three-dimensional photonic crystals, *Nature (London)* **609**, 925 (2022).
- [32] D. Schurig, J. J. Mock, B. J. Justice, S. A. Cummer, J. B. Pendry, A. F. Starr, and D. R. Smith, Metamaterial electromagnetic cloak at microwave frequencies, *Science* **314**, 977 (2006).
- [33] V. V. Klimov, A. A. Pavlov, D. V. Guzato, I. V. Zabkov, and V. D. Savinov, Radiative decay of a quantum emitter placed near a metal-dielectric lamellar nanostructure: Fundamental constraints, *Phys. Rev. A* **93**, 033831 (2016).
- [34] H. Chu, Q. Li, B. Liu, J. Luo, S. Sun, Z. H. Hang, L. Zhou, and Y. Lai, A hybrid invisibility cloak based on integration of transparent metasurfaces and zero-index materials, *Light Sci. Appl.* **7**, 50 (2018).
- [35] H. Tomita, K. Hashimoto, K. Takeya, and S. R. Tripathi, Development of a terahertz wave circular polarizer using a 2D array of metallic helix metamaterial, *Opt. Lett.* **46**, 2232 (2021).
- [36] J. Zhang, S. Zhou, X. Dai, M. Huang, and X. Yu, All-optical image edge detection based on the two-dimensional photonic spin Hall effect in anisotropic metamaterial, *Opt. Express* **31**, 6062 (2023).
- [37] S. Jahani and Z. Jacob, Transparent subdiffraction optics: Nanoscale light confinement without metal, *Optica* **1**, 96 (2014).
- [38] S. Jahani and Z. Jacob, All-dielectric metamaterials, *Nat. Nanotechnol.* **11**, 23 (2016).
- [39] A. Al Sayem, M. R. C. Mahdy, and Md S. Rahman, Broad angle negative refraction in lossless all dielectric or semiconductor based asymmetric anisotropic metamaterial, *J. Opt.* **18**, 015101 (2016).
- [40] S. Jahani, S. Kim, J. Atkinson, J. C. Wirth, F. Kalhor, A. Al Noman, W. D. Newman, P. Shekhar, K. Han, V. Van, R. G. DeCorby, L. Chrostowski, M. Qi, and Z. Jacob, Controlling evanescent waves using silicon photonic all-dielectric metamaterials for dense integration, *Nat. Commun.* **9**, 1893 (2018).
- [41] F. Wu, T. Liu, M. Chen, and S. Xiao, Photonic bandgap engineering in hybrid one-dimensional photonic crystals containing all-dielectric elliptical metamaterials, *Opt. Express* **30**, 33911 (2022).
- [42] G. Wei, B. Wang, K. Du, B. Zhang, C. Zhou, T. Wang, W. Han, W. Zhu, and S. Wang, Angle-insensitive transmission and absorption with a PT phase transition via coupled interface states in hybrid one-dimensional photonic crystal heterostructures, *Phys. Rev. A* **109**, 053504 (2024).
- [43] A. Poddubny, I. Iorsh, P. Belov, and Y. Kivshar, Hyperbolic metamaterials, *Nat. Photonics* **7**, 948 (2013).
- [44] L. Ferrari, C. Wu, D. Lepage, X. Zhang, and Z. Liu, Hyperbolic metamaterials and their applications, *Prog. Quantum Electron.* **40**, 1 (2015).
- [45] F. Wu, G. Lu, Z. Guo, H. Jiang, C. Xue, M. Zheng, C. Chen, G. Du, and H. Chen, Redshift gaps in one-dimensional photonic crystals containing hyperbolic metamaterials, *Phys. Rev. Appl.* **10**, 064022 (2018).
- [46] F. Wu, M. Chen, and S. Xiao, Wide-angle polarization selectivity based on anomalous defect mode in photonic crystal containing hyperbolic metamaterials, *Opt. Lett.* **47**, 2153 (2022).
- [47] A. H. M. Almwagani, M. Medhat, A. Mehaney, G. A. Ali, M. Irfan, and H. A. Elsayed, One-dimensional metamaterial photonic crystals comprising gyroidal and hyperbolic layers as an angle-insensitive reflector for energy applications in IR regions, *Eur. Phys. J. Plus* **138**, 483 (2023).
- [48] R. E. Hamam, I. Celanovic, and M. Soljačić, Angular photonic band gap, *Phys. Rev. A* **83**, 035806 (2011).
- [49] Y. Shen, D. Ye, L. Wang, I. Celanovic, L. Ran, J. D. Joannopoulos, and M. Soljačić, Metamaterial broadband angular selectivity, *Phys. Rev. B* **90**, 125422 (2014).
- [50] Y. Shen, D. Ye, I. Celanovic, S. G. Johnson, J. D. Joannopoulos, and M. Soljačić, Optical broadband angular selectivity, *Science* **343**, 1499 (2014).
- [51] Y. Shen, C. W. Hsu, Y. X. Yeng, J. D. Joannopoulos, and M. Soljačić, Broadband angular selectivity of light at the nanoscale: Progress, applications, and outlook, *Appl. Phys. Rev.* **3**, 011103 (2016).
- [52] Y. Qu, Y. Shen, K. Yin, Y. Yang, Q. Li, M. Qiu, and M. Soljačić, Polarization-independent optical broadband angular selectivity, *ACS Photonics* **5**, 4125 (2018).
- [53] J. Guo, S. Chen, and S. Jiang, Optical broadband angular filters based on staggered photonic structures, *J. Mod. Opt.* **65**, 928 (2018).
- [54] K. Yin, Y. Qu, S. E. Kooi, W. Li, J. Feng, J. A. Ratto, J. D. Joannopoulos, M. Soljačić, and Y. Shen, Enabling manufacturable optical broadband angular-range selective films, *ACS Nano* **15**, 19917 (2021).
- [55] Y. Gao, Z. Zhu, B. Zhang, J. Huangfu, L. Ran, and D. Ye, Tunable broadband angular selectivity for *s*-polarized terahertz incidences, *Appl. Phys. A* **127**, 127 (2021).
- [56] Y. Gao, B. Li, R. Wang, Q. Yan, J. Huangfu, and D. Ye, Polarization-independent broadband angular selectivity based on anisotropic diamagnetic metamaterial, *IEEE Trans. Antenn. Propag.* **70**, 7306 (2022).
- [57] M. E. Sasin, R. P. Seisyan, M. A. Kalitchevski, S. Brand, R. A. Abram, J. A. Yu. Egorov, A. P. Vasil'ev, V. S. Mikhlin, and A. V. Kavokin, Tamm plasmon polaritons: Slow and spatially compact light, *Appl. Phys. Lett.* **92**, 251112 (2008).
- [58] L. L. Missoni, G. P. Ortiz, and M. L. M. Ricci, Understanding the coupling between MIM cavities due to single and double Tamm plasmon polaritons, *Opt. Mater.: X* **20**, 100273 (2023).
- [59] Y. V. Konov, D. A. Pykhtin, R. G. Bikbaev, and I. V. Timofeev, Tamm plasmon polariton-based planar hot-electron photodetector for the near-infrared region, *Nanoscale* **16**, 9570 (2024).
- [60] M. F. Al-Kuhaili, Optical properties of hafnium oxide thin films and their applications in energy-efficient windows, *Opt. Mater.* **27**, 383 (2004).
- [61] W.-J. Kong, Z.-C. Shen, S.-H. Wang, J.-D. Shao, Z.-X. Fan, and C.-J. Lu, Graded index broadband antireflection coating prepared by glancing angle deposition for a high-power laser system, *Chin. Phys. B* **19**, 044210 (2010).

- [62] E. Palik, *Handbook of Optical Constants of Solids I* (Academic Press, San Diego, CA, 1985).
- [63] B. Wood, J. B. Pendry, and D. P. Tsai, Directed subwavelength imaging using a layered metal-dielectric system, *Phys. Rev. B* **74**, 115116 (2006).
- [64] P. Yeh, *Optical Waves in Layered Media* (Wiley, New York, 1988).
- [65] J. Li, L. Zhou, C. T. Chan, and P. Sheng, Photonic band gap from a stack of positive and negative index materials, *Phys. Rev. Lett.* **90**, 083901 (2003).
- [66] C.-K. Liu, S.-C. Chang, S.-W. Wang, and K.-T. Cheng, Privacy-protection system using a unidirectional emission waveguide liquid crystal display and an asymmetrical transmission window system, *Opt. Laser Eng.* **158**, 107175 (2022).
- [67] B.-F. Wan, H.-N. Ye, Y.-M. Ma, and H.-F. Zhang, Narrow-angle privacy protection based on anomalous propagation characteristic at epsilon-near-zero threshold frequency of $\text{YBa}_2\text{Cu}_3\text{O}_7$ ceramic material, *Ceram. Int.* **50**, 9089 (2024).
- [68] T. Gerfin and M. Grätzel, Optical properties of tin-doped indium oxide determined by spectroscopic ellipsometry, *J. Appl. Phys.* **79**, 1722 (1996).
- [69] C.-h. Xue, Y. Ding, H.-t. Jiang, Y. Li, Z.-s. Wang, Y.-w. Zhang, and H. Chen, Dispersionless gaps and cavity modes in photonic crystals containing hyperbolic metamaterials, *Phys. Rev. B* **93**, 125310 (2016).